LA-UR-13-28292
Approved for public release; distribution is unlimited.

Title: Muon Induced Fission Neutrons in Coincidence with Muon Tomography

Author(s): Bacon, Jeffrey D.
Borozdin, Konstantin N.
Fabritius, Joseph M. II
Morris, Christopher
Perry, John O.

Intended for: Report

Issued: 2013-10-28

Muon Induced Fission Neutrons in Coincidence with Muon Tomography

Jeffrey Bacon, Konstantin Borozdin, Joseph Fabritius, Christopher Morris, John Perry

Abstract

Cosmic-ray muons have several interactions in matter including scattering, ionization, and induced fission. We measure the muons directly through planes of drift tube detector modules. The secondary signals that result from muon induced fission, gammas and neutrons, can also be detected in coincidence with the cosmic-ray muon. Several detectors are studied for this purpose including: EJ-301 liquid scintillators, polyethylene moderated He-3 drift tubes, and solid plastics. For applications involving the detection of uranium and high Z objects, the EJ-301 detector yielded optimal results for measuring fast neutrons in coincidence with muon induced fission. Vertical muon imaging was compared with horizontal muon imaging showing similar image quality for equivalent time exposure.

Introduction

Most conventional radiography methods involve measuring the transmission of particles, e.g. x-rays, from attenuation processes. It has been shown that the scattering information, as in the case of muon tomography and charged particle radiography, can be used for imaging as well [1-14]. The common feature among all of these methods is the requirement for a detector that is located on the opposite side of the imaged object/plane with respect to the source of probing particles. In some scenarios, it may not be feasible to locate a detector in that configuration to measure the flux transmission. Thus, these scenarios require a single sided imaging technique whereupon the detector is placed between the source and the object of desire.

Single sided imaging has been used to look at the surfaces of objects, e.g. in airport security backscattering applications [15]; and single sided imaging has also been used to identify objects through photon backscatter and nuclear resonance fluorescence for homeland security applications [16-23]. These methods are either limited by penetration depth, or the steep increase in radiological dose required for obtaining useful imaging and isotopic information. By using cosmic-ray muons coincident with secondary signals such as fission neutrons, single sided imaging can be performed with high penetration and low dose. The tradeoff is that the natural muon flux is relatively low, ~10000 $\mu/m^2/min$, which requires longer integration time for imaging. Provided that an object is stationary, the use of cosmic-ray muons in these applications is an attractive alternative. Tagging cosmic-ray muons coupled with μ^- induced fission neutrons in coincidence enables us to detect and image SNM for warhead counting and treaty verification.

Our method is based on the use of signatures provided by interactions of cosmic-ray muons with an inspected object. As negatively charged muons stop, they are captured into atomic orbits in the stopping medium. In high-Z atoms, a stopped negative muon has a large probability of combining with one of the protons in a nucleus through the weak interaction forming an excited neutron and neutrino. In a fissionable material, stopped negative muons can trigger small fission chains, depending upon the effective multiplication of the neutronics system. Each fission reaction produces several gamma rays, 2-3 neutrons, and fission fragments. Products of this muon-induced fission create a distinctive signature that we can couple to muon trajectories in the target in order to create a tagged image within a coincidence window. In addition, cosmic-ray muons that pass through the target undergo Bremsstrahlung and pair-production resulting in potential photonuclear interactions.

The rate of stopped muons in small cubes (e.g. $1000\ cm^3$) of uranium that cause muon-induced fission is at most several a minute. The stopping rate varies with time, altitude and latitude, but in general is stable enough to produce a reliable probe. The rate of the secondary signal is directly proportional to the neutronics gain in the target. When compared to other sources of background, such as terrestrial gamma flux ($\sim 26000 \frac{\gamma}{m^2 s}$), the rate is low. Different detectors and techniques can be applied in order to see the muon-induced fission signal. These include: neutron detectors, e.g. liquid scintillators, gamma-ray detection with high energy thresholds, pulse-shape discrimination, and establishing a coincidence window.

The amount of fast and thermal fission events depends upon the geometry of the object, the quantity of fissile material, as wells as other materials that may reflect, absorb, or moderate neutrons. The Boltzmann transport equation defines these components through a series of losses and gains in the neutronics system [24]:

$$\begin{aligned}
&\left[\frac{1}{v}\frac{\partial}{\partial t} + \Omega \cdot \nabla + \Sigma_{\mathrm{t}}(r, E, t)\right] \phi(r, \Omega, E, t) \\
&= \int_0^\infty dE' \int_{4\pi} d\Omega' \Sigma_s(r, \Omega' \cdot \Omega, E' \to E) \phi(r, \Omega', E', t) \\
&+ \frac{\chi(E)}{4\pi} \int_0^\infty dE' \int_{4\pi} d\Omega' \nu(E') \Sigma_f(r, E', t) \phi(r, \Omega', E', t) \\
&+ Q(r, \Omega, E, t)
\end{aligned} \qquad \text{eq. 1}$$

If the system geometrical size is small, the neutron population will be dominated by losses due to leakage current, $[\Omega \cdot \nabla]\phi(r, \Omega, E, t)$. Losses can also include absorption through nuclear resonances and scattering out of a particular energy group, $\Sigma_{\mathrm{t}}(r, E, t)\phi(r, \Omega, E, t)$. If the resulting neutrons from fission are not fast enough, then fast fission neutronics gain is also diminished. These effects can have a significant impact on reducing the fast fission signal component that is being observed in coincidence with muon tracks. Of course, if neutrons of sufficient speed can remain in the fissile material for a long enough period of time, because of a large object size or adequate reflection, fast fission will occur, resulting in chain reactions that may be measured with neutron detectors. The source of these neutrons is defined by the scattering kernel $\int_0^\infty dE' \int_{4\pi} d\Omega' \Sigma_s(r, \Omega' \cdot \Omega, E' \rightarrow E)\phi(r, \Omega', E', t)$, the fission source term, $\frac{\chi(E)}{4\pi} \int_0^\infty dE' \int_{4\pi} d\Omega' \nu(E')\Sigma_f(r, E', t)\phi(r, \Omega', E', t)$, and any additional external sources, $Q(r, \Omega, E, t)$.

There is a practical challenge in measuring signals from fast or thermal fission. A fast signal resulting from muon-induced fission consists of neutrons and gammas emitted in a narrow time window on the order of hundreds of nanoseconds. However, if neutrons from thermal fission are to be measured, the timing coincidence window must be extended by hundreds of microseconds to account for the moderation time. The wider coincidence gate results in higher rate of accidental coincidences due to random background. This issue is further compounded if the neutron or gamma detectors are intrinsically slow.

There are several neutron energy regions that are important to consider for uranium isotope identification. A muon induced fission in uranium produces neutrons with energies that are well described by the Watt spectrum [25], with an average energy of 1-2 MeV and a tail above 10 MeV (see Figure 1). At the lower end of this fast spectrum (~1 MeV), the difference between fission cross-sections of uranium isotopes, U-238 and U-235, is almost two orders of magnitude, $\sigma_{f,U238} = 0.014\ b$ and $\sigma_{f,U235} = 1.2\ b$. At the higher end of the spectrum (above ~5 MeV), the difference in fission cross-section becomes smaller, e.g. at 15 MeV $\sigma_{f,U238} = 1.2\ b$ and $\sigma_{f,U235} = 2.1\ b$. Another neutron energy region to consider is the thermal one, where the difference between isotopes becomes dramatic, with U-235 fission cross-section being over 7 orders of magnitude larger than U-238, e.g. $\sigma_{f,U238} = 1.7 \cdot 10^{-5}\ b$ and $\sigma_{f,U235} = 590\ b$ at 0.025 eV. The U-235 and U-238 total fission cross-sections are shown in Figure 2.

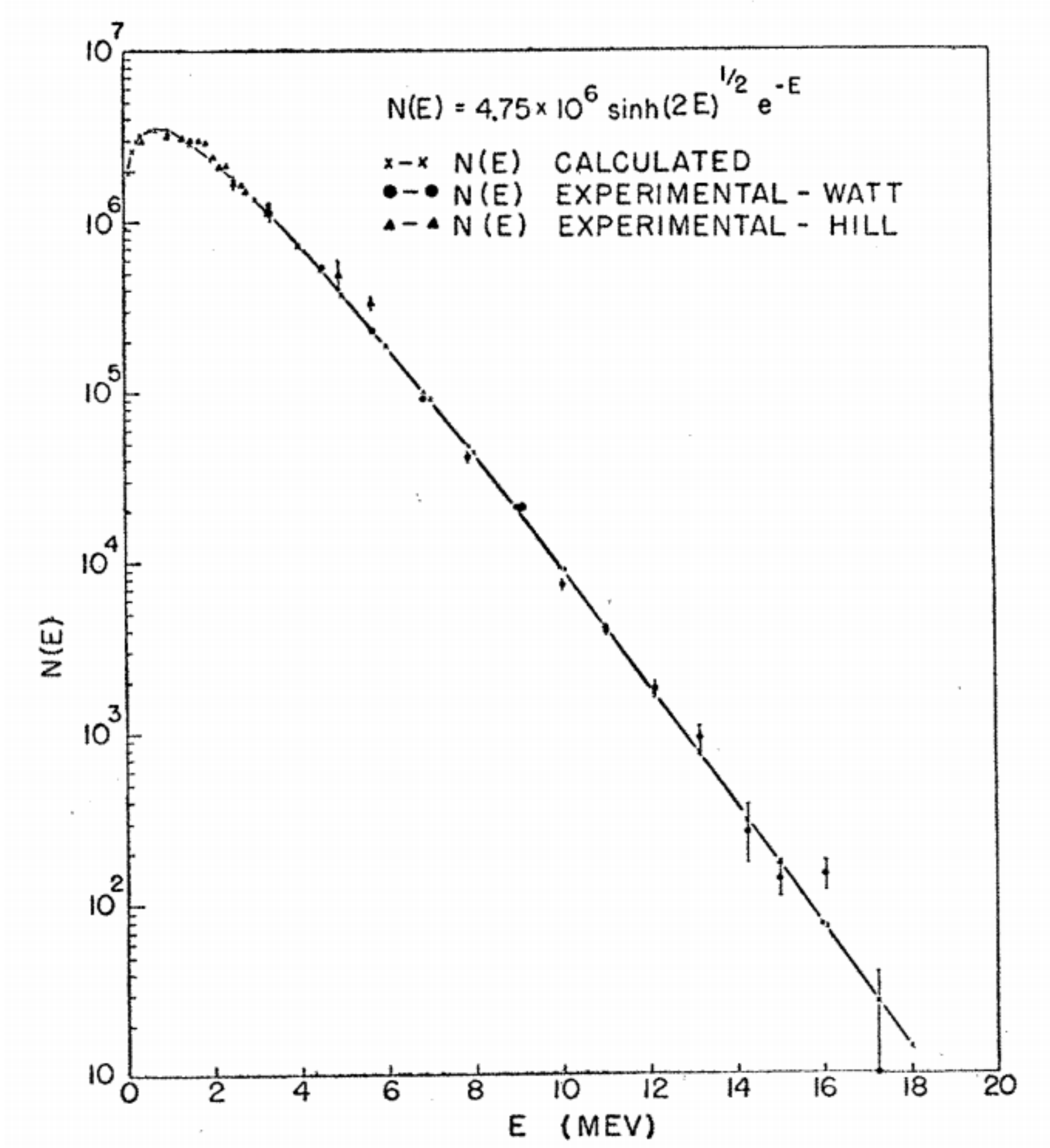

Figure 1 – Energy spectrum of fission neutrons. The calculated curve is based on the assumption of a Maxwellian distribution in the center-of-mass system for the neutrons emitted by a fission fragment [25].

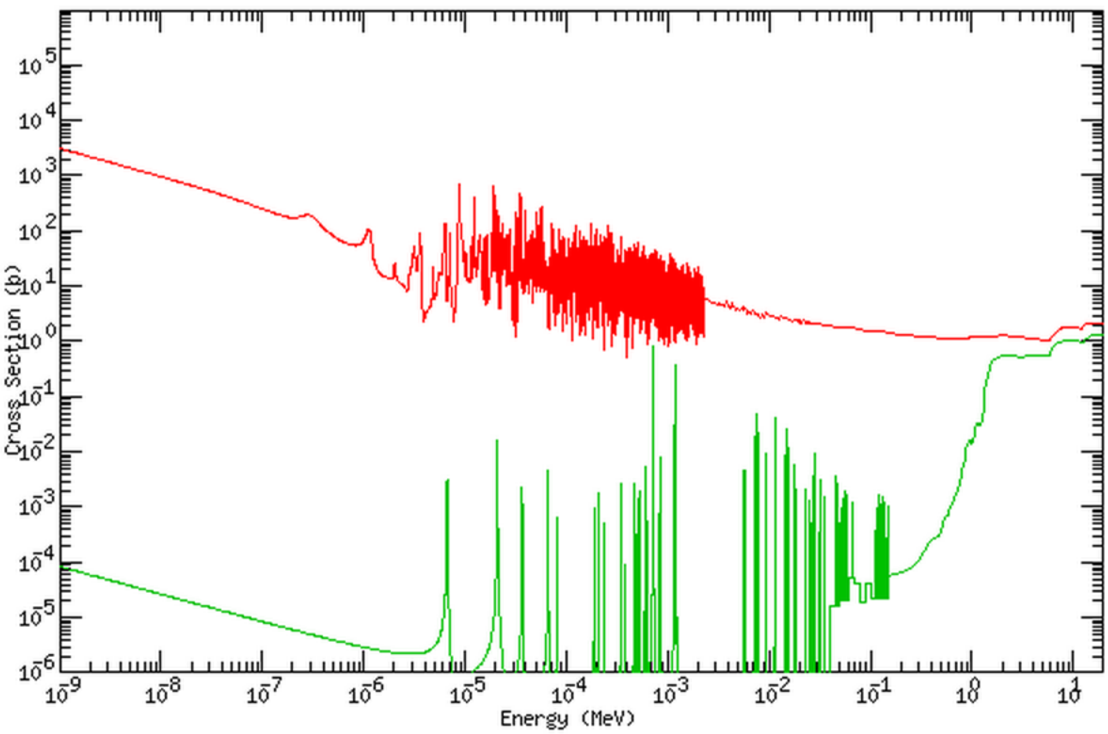

Figure 2 – Total fission cross-sections of uranium. U-235 is shown in red and U-238 is shown in green. There are three regions of interest for muon induced fission. The first is the region above 10 MeV where the difference in fission cross-section is small between U-235 and U-238. The second is the region around 1-2 MeV where the U-235 cross-section begins to become larger than U-238. Finally, the third region is at thermal energies where the U-235 cross-section is very large (data from ENSDF [26]).

Geant4 HEU, LEU, and DU Cube Simulation Study for Muon Induced Fission

Geant4 is used to simulate the multiple physical processes that occur in muon induced fission. This is done by separating the muon induced fission process into several stages. First, the neutronics of three bare cubes, HEU, LEU, and DU are investigated. The HEU, LEU, and DU cubes have a side length of 10cm. The neutronics study is performed using fast and thermal neutrons in order to understand the outgoing neutron and gamma flux from fission. Second, a simulation is performed on the LEU cube surrounded by an inch of high density polyethylene moderator (HDPE). The HDPE affects the timing distribution of secondary signal neutrons, spreading them over several milliseconds and ultimately reducing the effectiveness of tagged muon radiography. Finally, the interactions of μ^+ and μ^- with the three cubes tie together the neutronics with the muon induced fission.

Neutrons of different energies are simulated within a cube of HEU, LEU, or DU. The output of the simulations is plotted to show the energy and time distributions in order to better understand the detector coincidence window sizes and rates. Several energy regions are investigated corresponding to the expected neutron energies that occur from muon-induced fission. The fission simulations produce a Watt spectrum in uranium that contains U-235 with a spatial distribution proportional to the neutron mean free path. A 4π spherical detector covering the entire solid angle with a radius of 30 cm is used to measure the distribution of particles emitted from each cube (see Figure 3). The high-precision *Neutron_HP* model is used to simulate the neutrons below 20 MeV accurately in Geant4 [27-31].

The following simulation runs used 1 million particles per case in order to study the energy and timing distribution of secondary signals with adequate statistics. Simulations were performed with an isotropic neutron source located at the center of the uranium. Neutron source energies were monochromatic at either 15 MeV or 0.025 eV. The uranium cubes were bare. The integrated results of the simulation are shown in a table following individual discussions of each component of the flux.

The gamma energy spectra for the bare cube simulations are shown in Figure 4. The HEU signal is stronger than the signal found in either the LEU or DU, which is to be expected due to the higher fission cross-section found in U-235. The average energy of the exiting gamma rays from fission and capture processes is between 1-2 MeV, with the spectrum extending beyond 8 MeV.

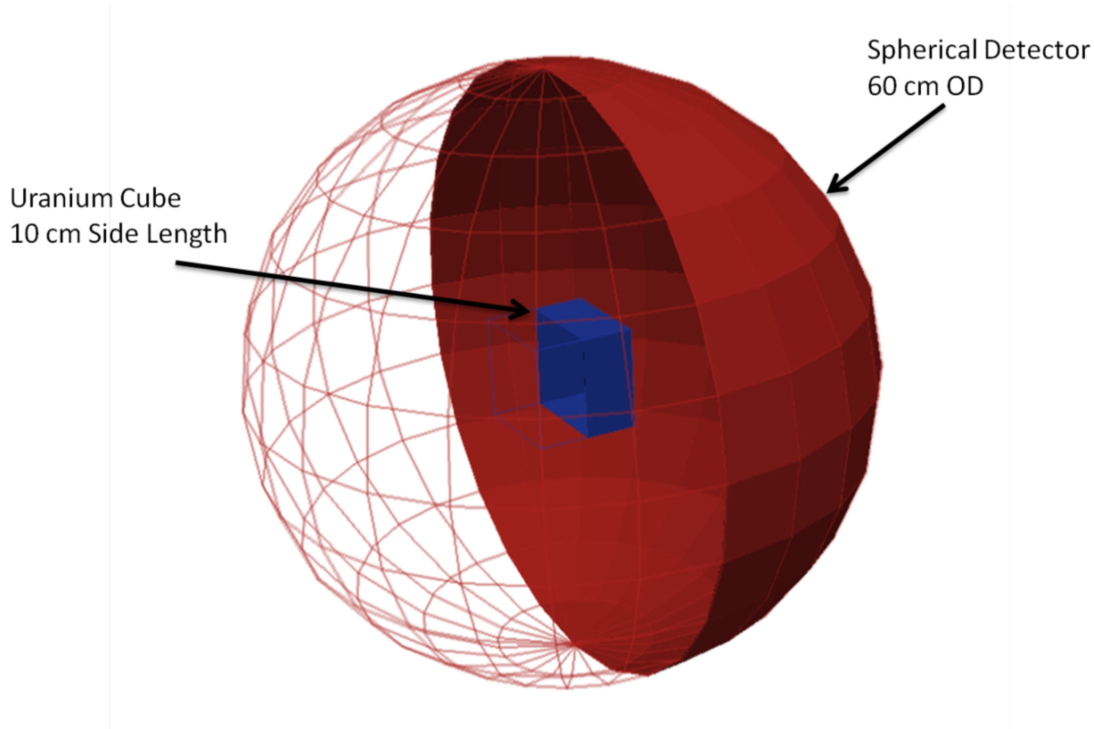

Figure 3 – Geant4 simulation geometry of a uranium cube with a 4π spherical detector surface. The spherical detector is sensitive to gamma and neutron flux that results from fission and other processes. This was used to study the neutronics output of different uranium enrichments with muon and neutron sources.

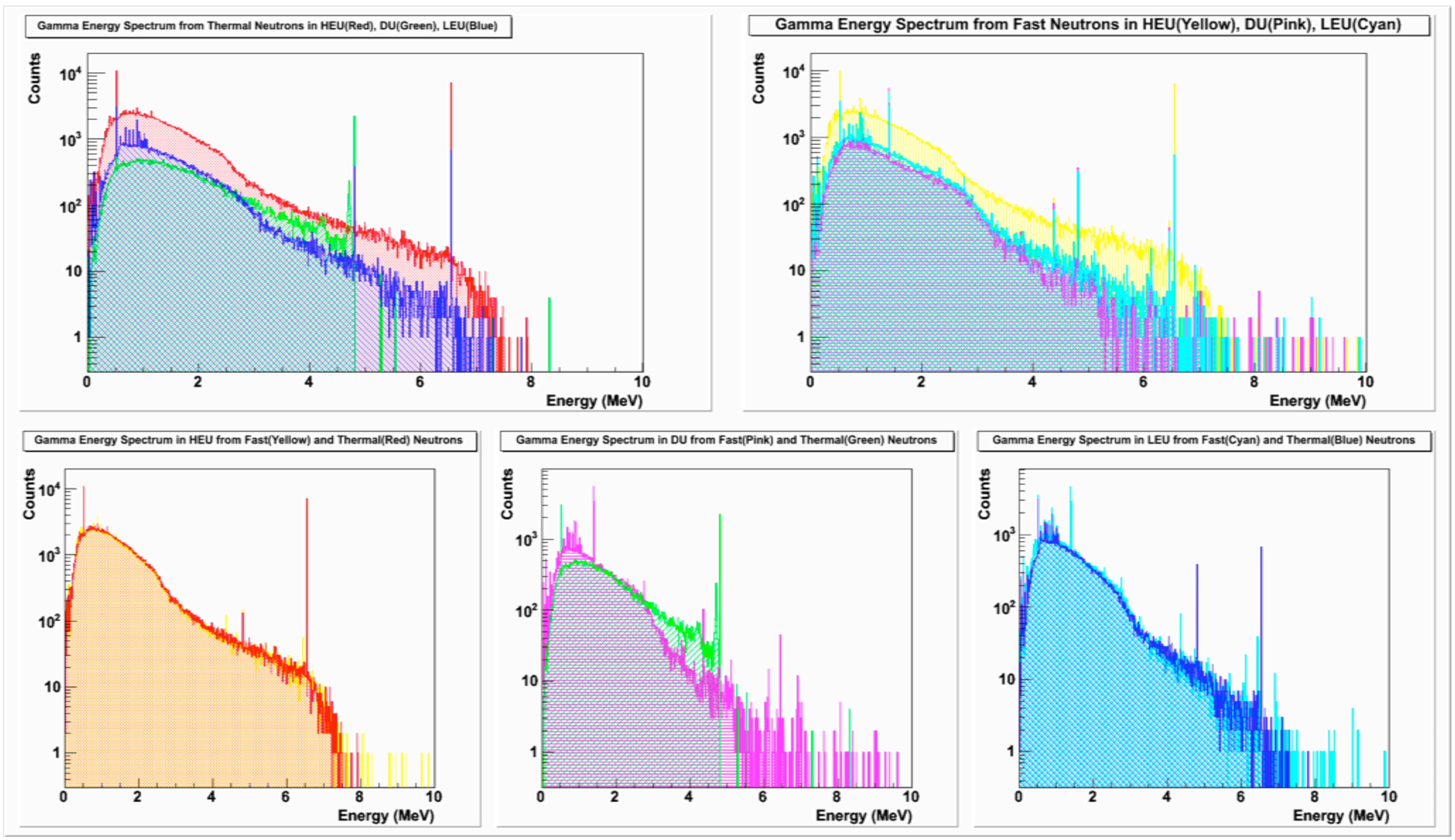

Figure 4 – Neutronics simulation of three uranium cubes consisting of depleted uranium, 19.5% U-235 low enriched uranium, and 90% U-235 high enriched uranium. A thermal neutron and fast (15 MeV) neutron point source was used in each cube. The secondary gamma energy spectra are compared. Several differences are immediately noticeable, first the overall yield of the gamma is larger in the HEU as would be expected by the larger fission cross-section of U-235. In DU, there is a

The temporal distribution of the gamma events resulting from the capture and fission of thermal and fast neutrons is shown in Figure 5. The thermal neutrons stimulate fissions quickly in LEU and HEU, producing secondary gamma-rays at the times shorter than 10 microseconds. The thermal neutrons in DU scatter for a longer period of time prior to their capture and release of gamma rays. In the fast energy range, the gammas can be seen largely as a result of fast fission. Delayed gammas are also visible, but they are not useful for muon tagged radiography due to their much later occurrence in time. A coincidence window for prompt gamma detection from muon induced fission should be set below 10 microseconds.

The energy spectra of the neutron flux resulting from the capture and fission of thermal and fast neutrons in the LEU, DU, and HEU cubes are shown in Figure 6. In DU, the escaping thermal neutrons have a broadened energy from upscattering and downscattering. The LEU and HEU show a typical Watt spectrum resulting from thermal fission. The fast neutrons also show a Watt fission spectrum that is softened by the DU in the cube. Additionally, the 15 MeV neutron source escape peak is also present in the energy plot. The secondary neutron detection from muon induced fission involves measuring polychromatic neutrons, covering the Watt spectrum.

The timing spectra of the neutron flux resulting from fission of thermal and fast neutrons in HEU, LEU, and DU cubes are shown in Figure 7. In DU, the thermal neutrons that escape reach the detector much later than the fission neutrons in the LEU and HEU cube. For both fast and thermal fission in the LEU and HEU cubes, the prompt neutrons are measured within several microseconds. The measurement of delayed neutrons is possible, but according to the timing distribution, this measurement would require a prohibitively large coincidence window. For the accidental background suppression the coincidence window for measuring secondary neutrons from muon-induced fission must be closed within several microseconds of the fission event.

The neutronics analysis is concluded with one final study that describes the timing spectrum of secondary gammas and neutrons when moderation is present. The geometry consists of the LEU cube (10 cm on a side) surrounded by 5 cm of high density polyethylene (HDPE). Neutrons are generated as an isotropic point source in the center of the cube with thermal or fast energies. The timing and energy spectra of the secondary neutrons and gammas from the moderated LEU cube are shown in Figure 8. The HDPE extends the time until neutron detection from several microseconds to milliseconds.

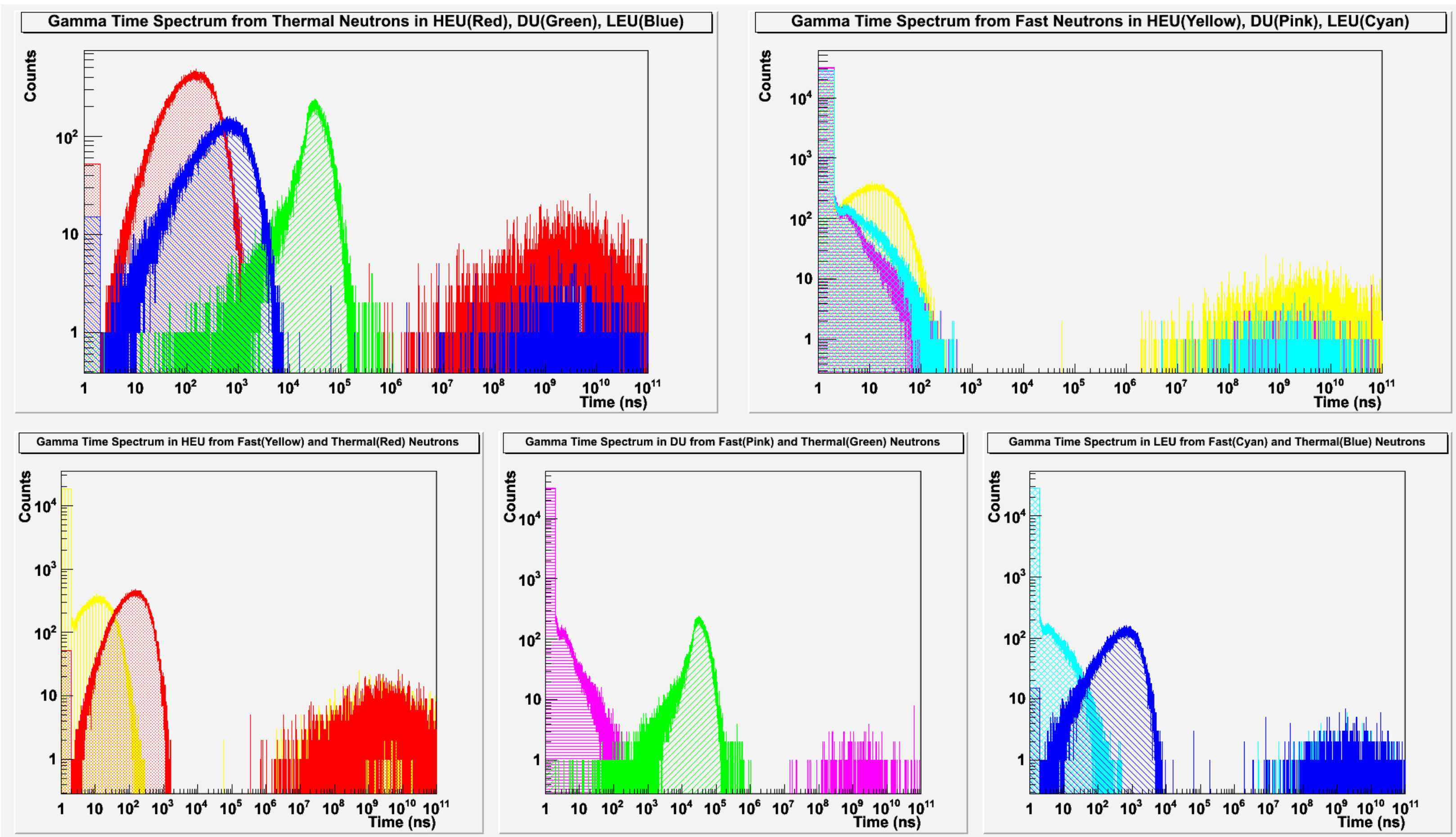

Figure 5 – Neutronics simulation of three uranium cubes consisting of depleted uranium, 19.5% U-235 low enriched uranium, and 90% U-235 high enriched uranium. A thermal neutron and fast (15 MeV) neutron point source was used in each cube. The secondary gamma time distributions are compared. The thermal neutrons fission quickly in LEU and HEU, which results in secondary gamma time distributions below 10 microseconds. The thermal neutrons in DU scatter for a longer period of time

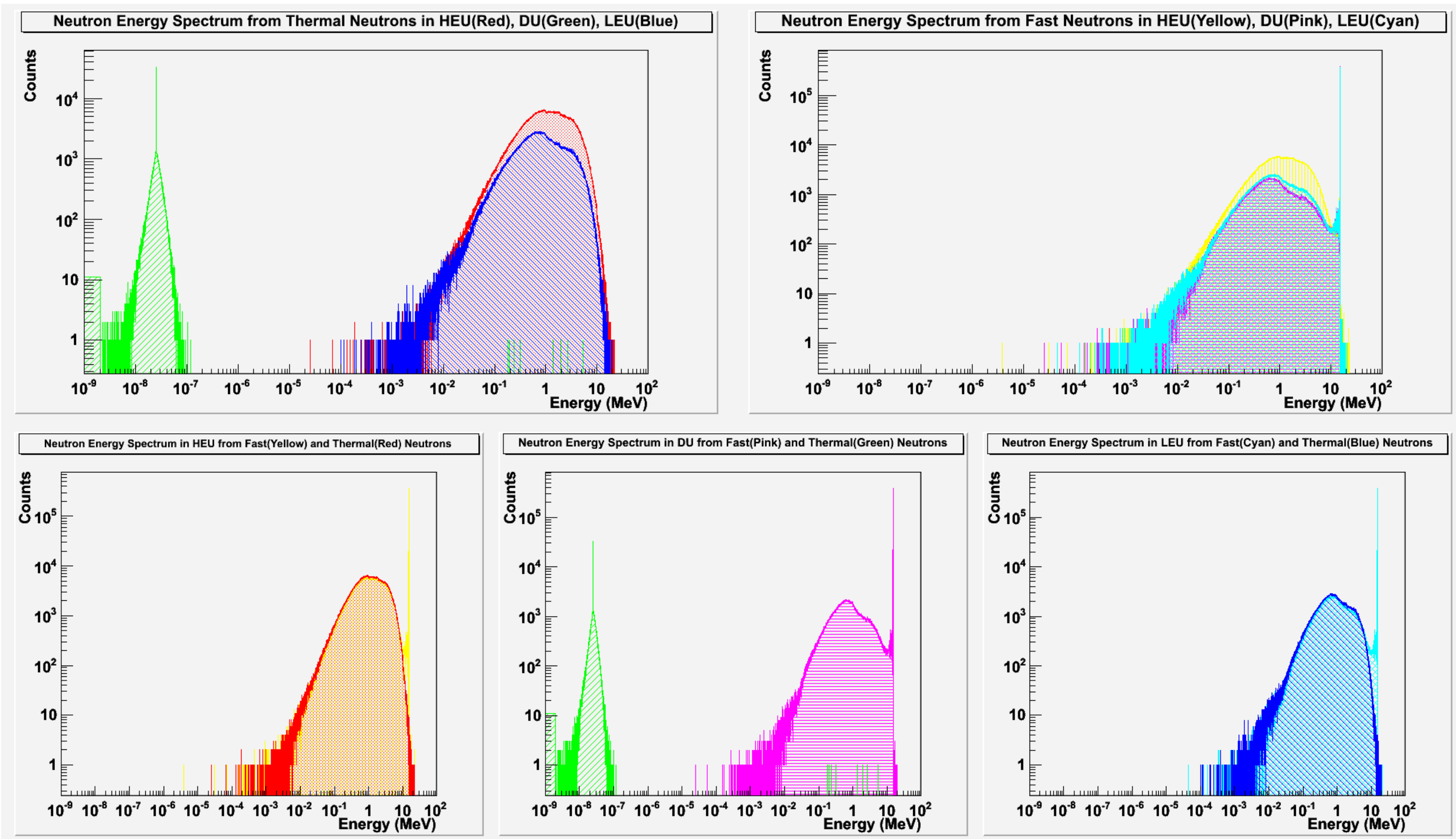

Figure 6 - Neutronics simulation of three uranium cubes consisting of depleted uranium, 19.5% U-235 low enriched uranium, and 90% U-235 high enriched uranium. A thermal neutron and fast (15 MeV) neutron point source was used in each cube. The secondary neutron energy spectra are compared. In DU, the thermal neutrons that escape have a broadened energy from upscattering and downscattering. The LEU and HEU show a typical Watt spectrum resulting from thermal fission. The fast neutrons also show a Watt fission spectrum that is softened by the concentration of DU in the cube. Additionally, the 15 MeV source neutron is also seen at the upper part of the energy plot.

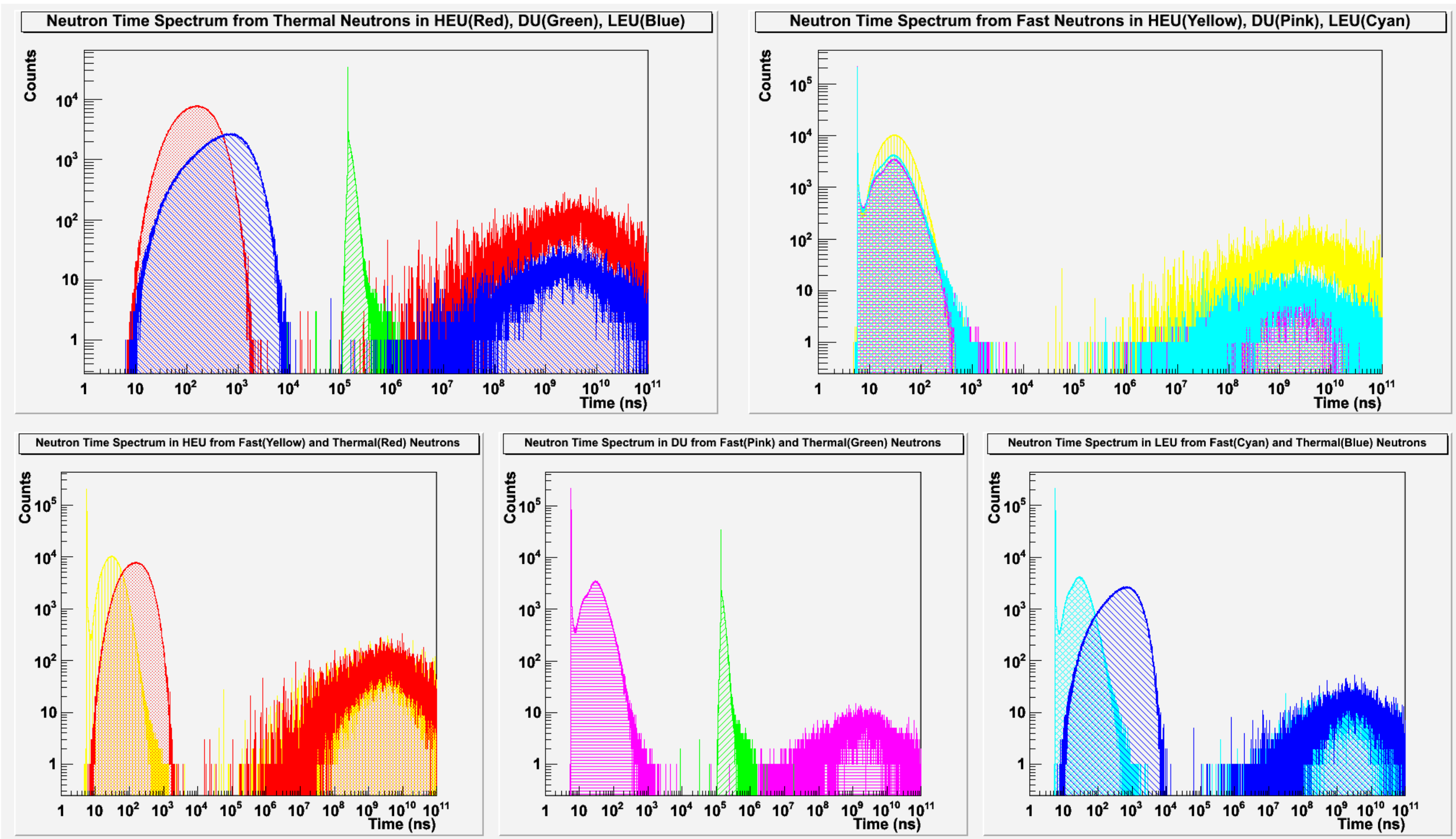

Figure 7 - Neutronics simulation of three uranium cubes consisting of depleted uranium, 19.5% U-235 low enriched uranium, and 90% U-235 high enriched uranium. A thermal neutron and fast (15 MeV) neutron point source was used in each cube. The secondary neutron timing distributions are compared. In DU, the thermal neutrons that escape reach the detector much later than the fission neutrons in the LEU and HEU cube. For both fast and thermal fission in the LEU and HEU cubes, the prompt neutrons are measured within several microseconds. Additionally, the delayed neutrons are visible but not important for purposes of measuring muon induced fission.

A thermal neutron coincidence window would need to span several milliseconds, significantly increasing the background count rate and therefore decreasing the signal-to-noise ratio of muon induced fission and tagged radiography. For the same reason the signal-to-noise ratio is also reduced in moderated neutron detectors, such as HDPE wrapped He-3. The most promising solution to this problem is to utilize fast liquid scintillators with good pulse-shape discrimination characteristics in order to measure fast neutrons. This was done after several experimental studies that investigated several detectors including: HDPE moderated He-3, He-4, lithium, and liquid scintillators. The experimental results shown in this dissertation are from the EJ-301 liquid scintillators.

Following the neutronics study in the different uranium cubes, several simulations were performed using μ^- and μ^+ distributed uniformly throughout cubes of DU, LEU (19.5% U-235), and HEU (90% U-235). A parametric study of two muon energies, 2 GeV and 1 MeV, was performed. The higher muon energy approximately represents the average energy of the cosmic-ray muon spectrum. These muons lose energy in matter slowly, primarily through ionization. In the lower energy range, the muons stop in thin layers of material due to the increase in their energy losses, dE/dx. The output of the parametric simulation predicts the secondary neutron and gamma-ray rates measured in a 4π detector per muon generated. By using Geant4, it is shown that both μ^- and μ^+ produce secondary particles in uranium. At lower energies, the μ^- slows down rapidly and stops with a high probability of capture in the uranium. This process is simulated by the *muMinusCaptureAtRest* process in Geant4, and produces secondary particles and additional fissions. Secondary particles in uranium can also be created by photonuclear processes caused by cosmic-ray muon Bremsstrahlung.

The stopping of μ^- in uranium cubes (10 cm side length) is shown in Figure 9. This primarily results in muon induced fission with secondary neutrons and gammas that are released proportional to the amount of U-235 enrichment, which enhances the neutronics gain of the cube. The muon induced fission that occurs from stopped μ^- produces a signal that is dependent on neutronics gain. This signal can be useful for treaty verification applications. The signal rates per stopped muon are shown in the table at the end of this section.

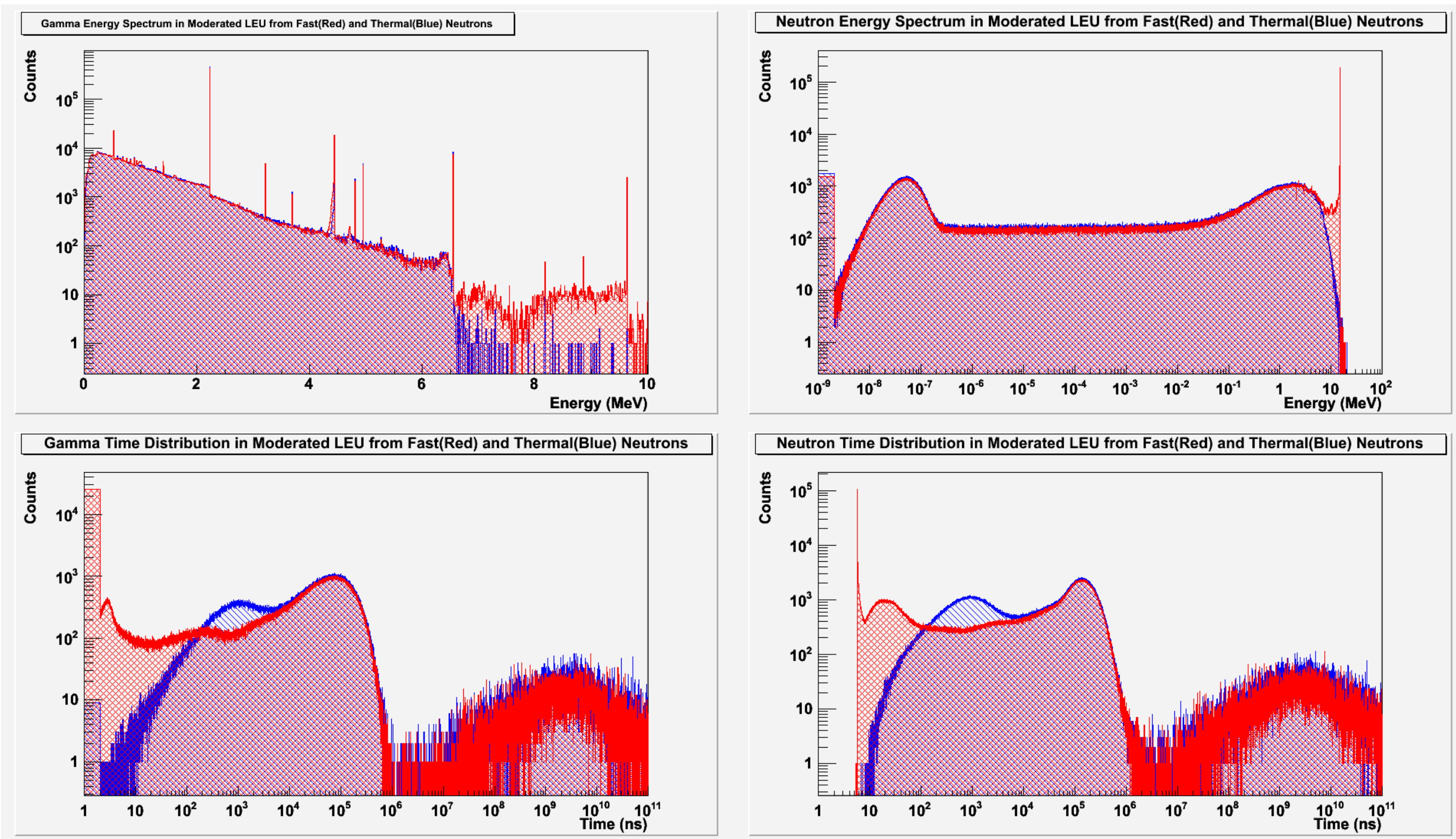

Figure 8 – A study of moderation times for fission in LEU using Geant4. A point source of thermal and fast (15 MeV) neutrons was simulated in the center of the LEU (10 cm side) cube. The LEU was surrounded by 5 cm of HDPE on each side. The most significant issue is that the secondary signals are stretched out to several milliseconds from the initial event. For muon induced fission tagged radiography purposes, this results in a coincidence window that is too large.

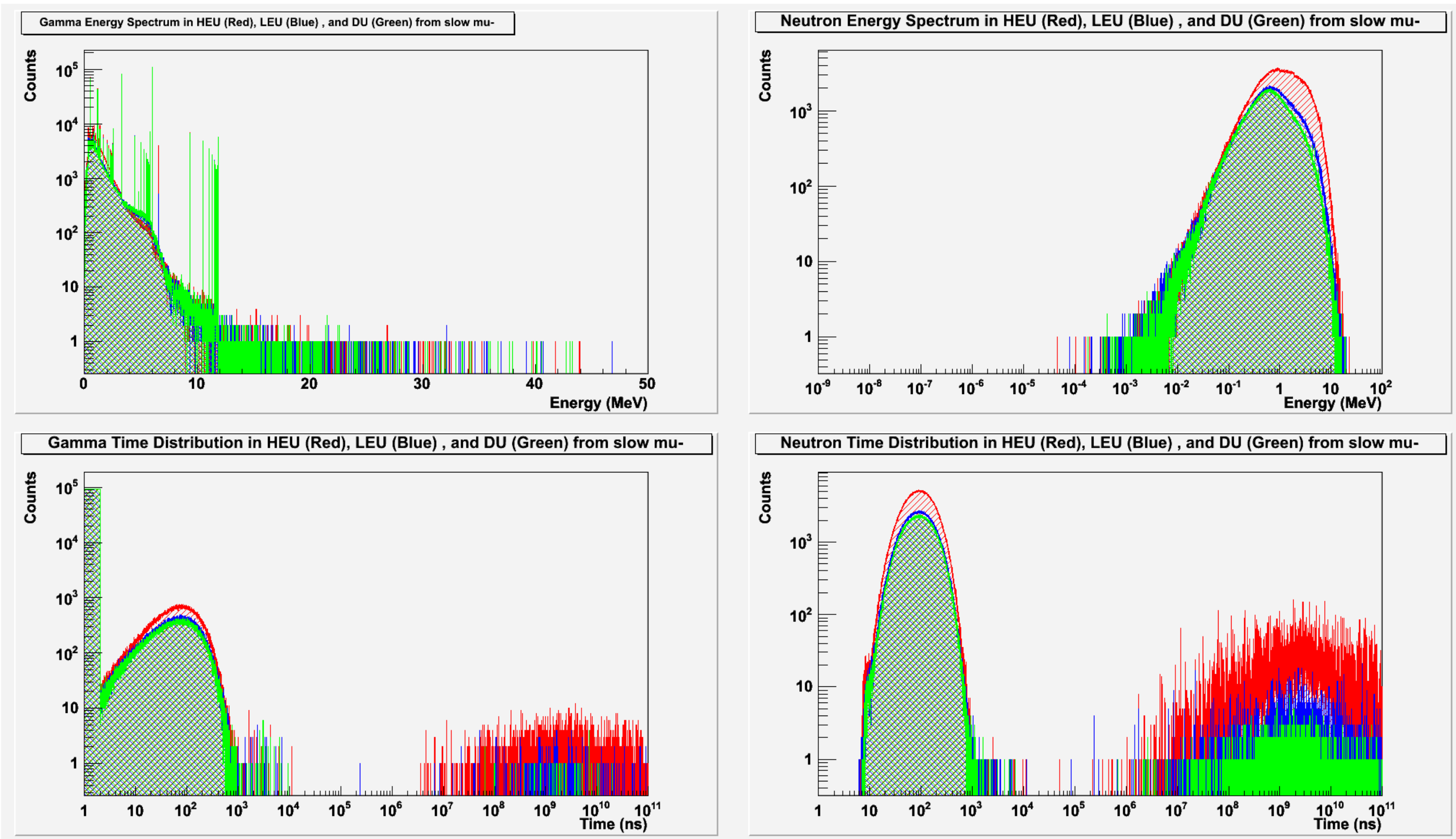

Figure 9 – Secondary neutron and gamma energy spectrum that result from μ^- stopping in cubes of uranium: HEU (red), LEU (blue), and DU (green). The primary mode of neutron generation is due to muon induced fission from μ^- capture. Two important features are 1) more gain for increasing U-235 concentration and 2) the secondary prompt signals occur below 1 microsecond.

Fast cosmic-ray muons of both charges and slow μ^+ generate secondary neutrons at much lower rates compared to μ^- induced fission. For example, if a slow μ^+ stops in uranium it decays releasing a fast positron and neutrinos. The positron creates photons through Bremsstrahlung, which may result in photonuclear production of neutrons. Additionally, fast muons may also radiate photons from Bremsstrahlung in high-Z targets. The rates of these effects are much smaller (by several orders of magnitude) when compared to μ^- induced fission. Figure 10, Figure 11, Figure 12 show that prompt neutrons are produced by these processes, but at a much smaller frequency.

The conclusion of this study is that the μ^- induced fission produces a dominant source of neutrons as compared to the other processes. Additionally, the increased neutronics gain found in the HEU provides increased secondary signal that is useful for tagged radiography. By using this additional signal, materials with high neutronics gain can be tagged and located. As was shown, both neutrons and gammas are useful signals for this method. We have determined that neutrons are a more desirable secondary signal to measure for several reasons: 1) the gamma background is large, 2) low-energy gamma-rays are self-shielded in SNM, and 3) the majority of the secondary neutron signal is the result of μ^- fission events.

The rates of secondary neutrons in the three different cubes are shown below. These rates refer to the prompt neutrons measured within 1 μs of the muon either passing through or stopping in the uranium cubes. As will be shown in the next section, this time frame corresponds to the prompt signal measured by the EJ-301 liquid scintillator detectors. The rates were determined by using the simulations mentioned previously in this section: 1 million incident muons, uniform source distribution, three types of uranium cubes, two muon speeds, two muon charges, and a 4π detector. The majority of the secondary neutron signal is emitted from the muon induced fission process induced by slow μ^-. The HEU U-235 enrichment results in an increase of neutron output by a factor of two compared to the LEU. The difference between neutron output in DU and LEU is much smaller. Theoretically, it may be possible to differentiate DU from LEU as there is a 15 percent difference in the neutronics gain.

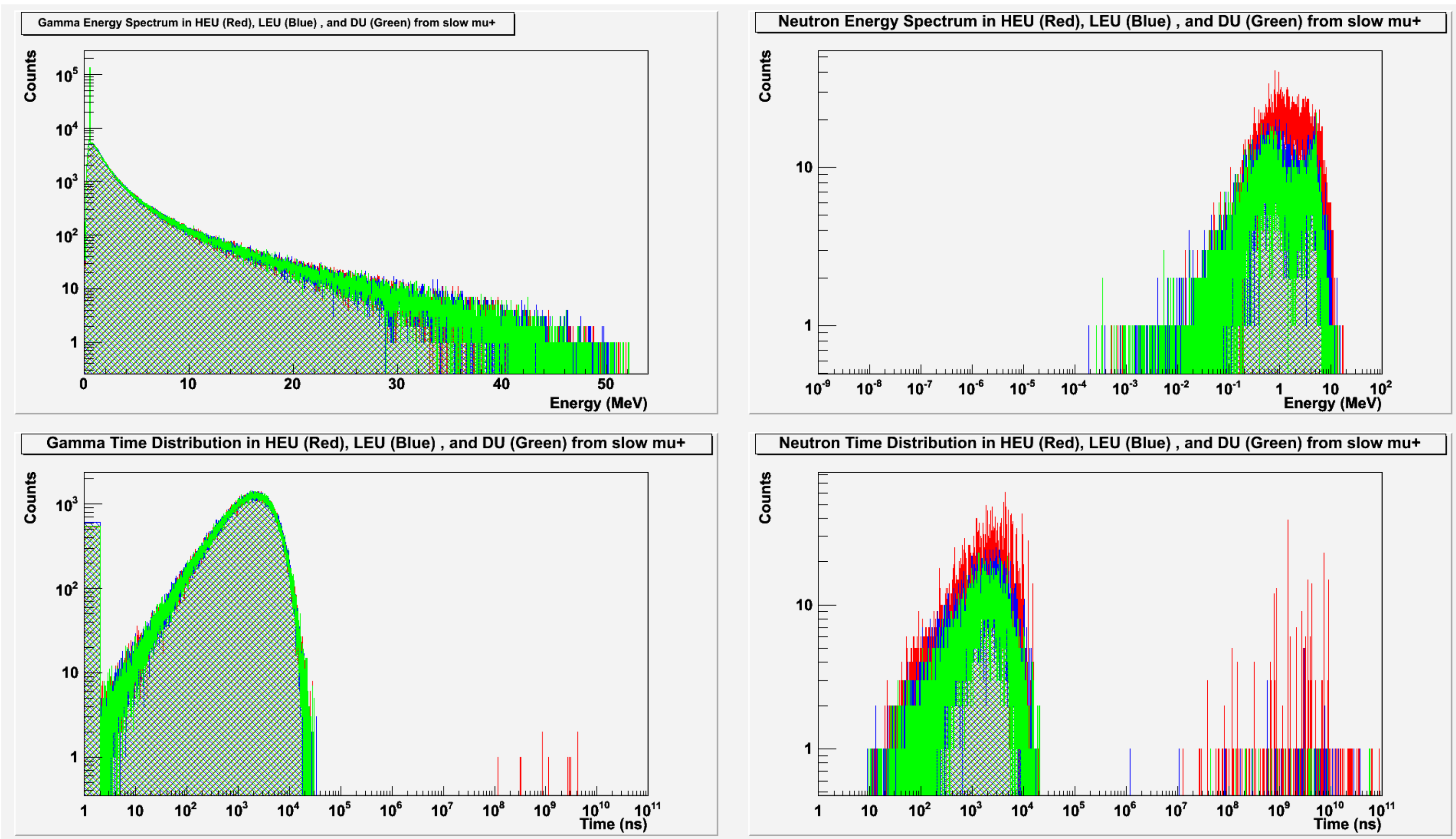

Figure 10 - Secondary neutron and gamma energy spectrum that result from μ^+ stopping in cubes of uranium: HEU (red), LEU (blue), and DU (green). The primary mode of neutron generation is due to μ^+decay resulting in a fast positron that yields a Bremsstrahlung photon and subsequent photonuclear processes. There is a small increase in neutronics gain when comparing the HEU to the other cubes.

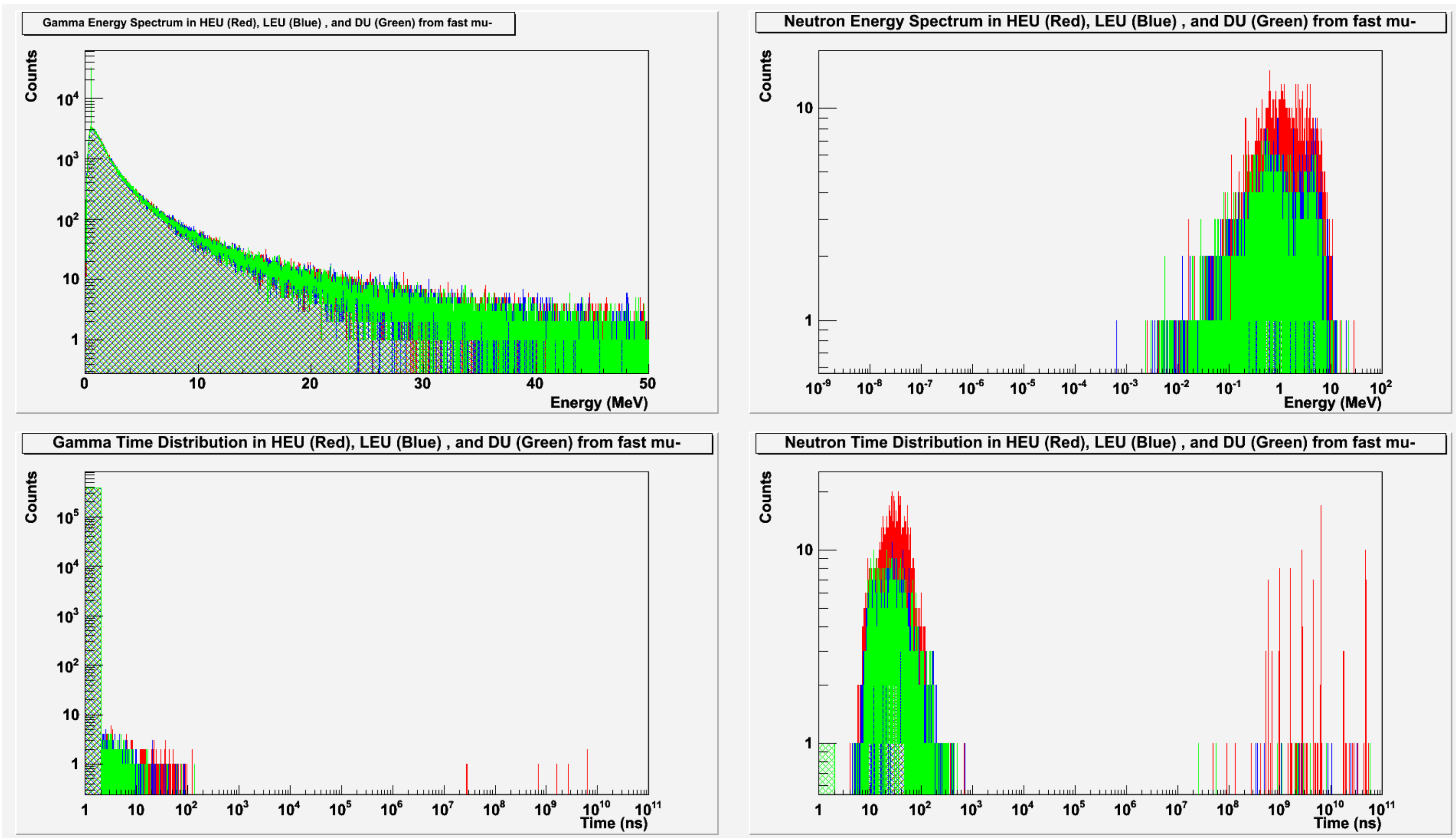

Figure 11 - Secondary neutron and gamma energy spectrum that result from fast μ^- passing through cubes of uranium: HEU (red), LEU (blue), and DU (green). The primary mode of neutron generation is due to direct μ^- Bremsstrahlung photon production and subsequent photonuclear processes. There is a small increase in neutronics gain when comparing the HEU to the other cubes.

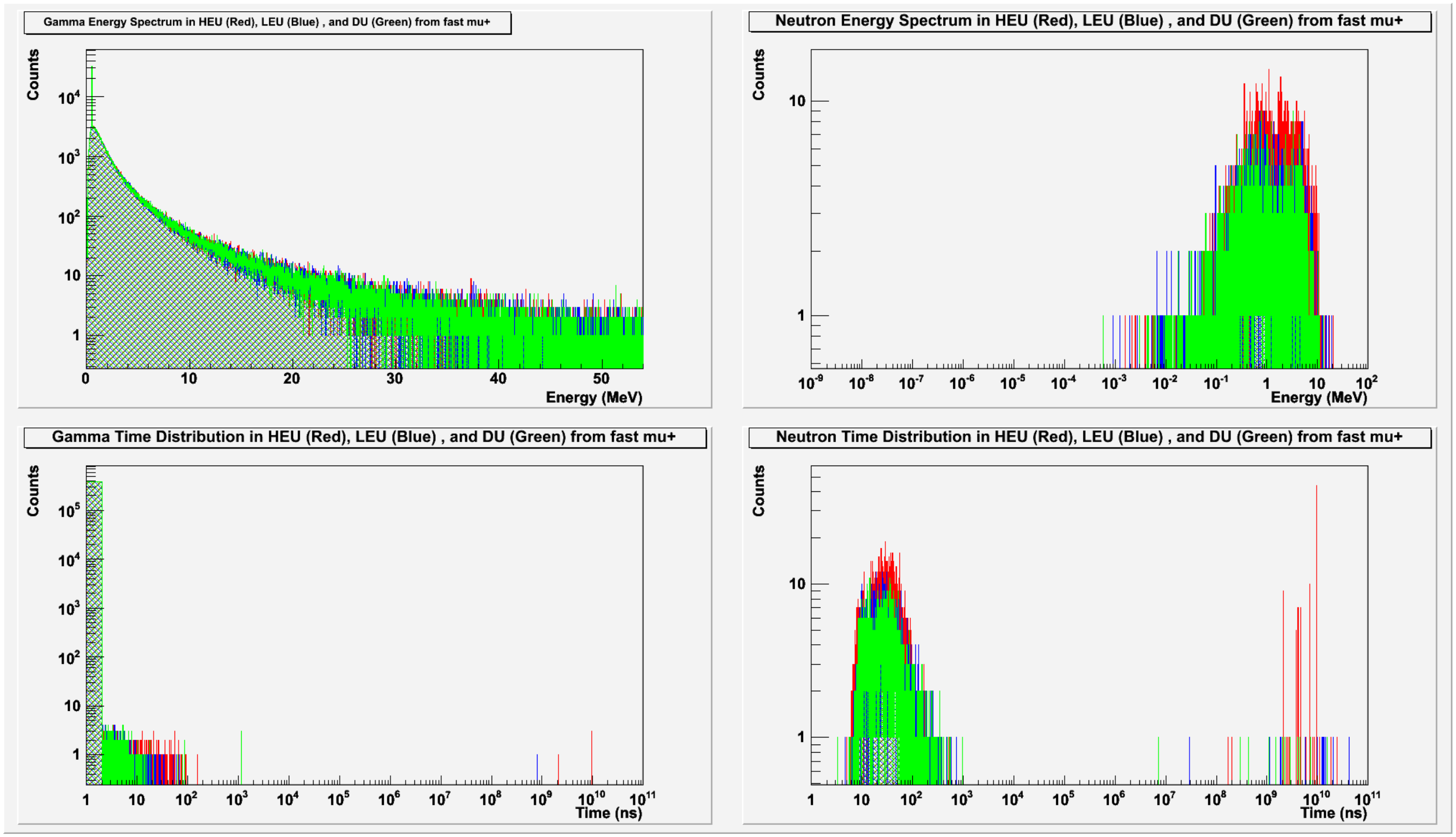

Figure 12 - Secondary neutron and gamma energy spectrum that result from fast μ^+ passing through cubes of uranium: HEU (red), LEU (blue), and DU (green). The primary mode of neutron generation is due to direct μ^+ Bremsstrahlung photon production and subsequent photonuclear processes. There is a small increase in neutronics gain when comparing the HEU to the other cubes. The difference between μ^+ and μ^- neutron production is minimal.

	Fast Neutrons/Incident Muon		
	DU	**LEU**	**HEU**
slow mu-	1.64E+00	1.88E+00	3.60E+00
slow mu+	4.07E-03	4.84E-03	8.24E-03
fast mu-	3.25E-03	3.54E-03	7.14E-03
fast mu+	3.53E-03	3.76E-03	6.27E-03

Table 1 – Rate of fast neutrons that are emitted from bare cubes of uranium (10 cm on a side): HEU (90% U-235), (19.5% U-235), and DU (0% U-235). The majority of secondary neutron signal is emitted from the muon induced process induced by slow μ^-. The HEU results in an increase of neutron output by a factor of two compared to the The difference between DU and LEU is much smaller.

Secondary Signal Detection: Why we chose EJ-301

The secondary signals used to tag muon induced fission for muon radiography result from neutrons and gammas born during the fission process. Several detectors were investigated for measurement of these fission products. There were several criteria used to determine the feasibility of each detector: time until detection, efficiency, and susceptibility to background. As will be discussed in the muon induced fission chapter, the neutron is the best secondary particle to detect for tagged muon induced fission radiography. Thus, the focus on secondary particle detection is specific to the identification of a neutron in coincidence with the incident muon.

Several detectors were evaluated: He-3 tubes wrapped in polyethylene, He-4 tubes, a solid plastic scintillator bar, and EJ-301 liquid scintillators; these detectors are shown in Figure 13. The solid plastic scintillator bars failed at providing a signal of neutron flux due to having poor pulse shape discrimination characteristics and a large gamma background detection rate. The He-4 tubes were also not suitable given that their efficiency was at most 1-2 percent for detection of fast neutrons. The He-3 tubes wrapped in polyethylene performed well; however, their time until detection was too long due to moderation time which lowered the signal to noise ratio. The EJ-301 liquid scintillators were the best candidates for identifying neutrons in coincidence with the incident cosmic-ray muon with the best signal to noise ratio.

Figure 13 – Detectors used to measure neutrons from muon induced fission. There were several criteria for identifying the best neutron detector: time until detection, efficiency, and susceptibility to background (mainly gamma). The two best detector candidates were the liquid scintillator and the He-3 polyethylene wrapped suitcase detector.

Measuring Muon Induced Fission with the Moderated He-3 Suitcase and Scintillator Bars

The thermalized neutrons were detected by a “suitcase” of He-3 tubes wrapped in polyethylene. The polyethylene provides the moderator to thermalize the neutrons. The He-3 has a high cross-section for the neutron inelastic scattering which ultimately yields signal. These neutrons are slow by the time of detection (order of 10s to 100s of microseconds time of flight). The large coincidence window negatively impacts the signal to noise ratio for comparing neutrons that result from the muon induced fission with the incident muon tracks. Scintillator bars were used to detect both the gamma and fast neutron signal. These scintillators were a solid plastic with a PMT attached on each end of the bar. The bars were fed into the MMT TDCs with a high gain and low discriminator in order to obtain the lower light yield neutron counts along with the gamma signatures. Unfortunately, the lack of pulse shape discrimination and the high gain/low threshold resulted in a poor signal to noise ratio performance. The solution (as shown further in the report) is to use fast neutron detectors with pulse shape discrimination as they offer a good efficiency (~15-30 %) and fast timing resolution (less than 100s of ns).

Figure 14 shows a LEU block in a polyethylene doghouse (4 inch floor, 2 inch walls). Secondary signals were measured the He-3 “suitcase” neutron detector located 3 inches above the LEU with a boron loaded foam shield on top of the detector. The poly doghouse moderated the neutrons for optimal detection efficiency in the He-3 tubes. The solid angle of the “suitcase” detector is large given its proximity to the He-3 tubes. The plastic and the LEU cube’s steel cladding cuts down on secondary sources of radiation that may originate from the LEU cube due to Beta rays.

In Figure 15, the LEU cube is placed at an optimal location in the center of the “suitcase” detector. By utilizing the increased solid angle we obtain a clear filtered radiograph of the LEU. Additionally, the plastic in the “suitcase” detector helps to reflect thermalized neutrons and may give increased neutronics gain per fission event, though the timing of these events may extend into the millisecond range.

Figure 16 is a radiograph of the LEU cube and the DU plates (with a volume similar to the LEU cube). The image on the left is the stopped track radiograph which shows two similar peaks due to the nearly identical object volumes and densities found in the LEU cube and the DU plates. The image on the right is the filtered radiograph using the He-3 “suitcase” detectors. The higher neutronics gain of the LEU produces more secondary signals that are in coincidence with the muon stopped tracks.

In Figure 17, we compare the LEU cube and DU plates (similar mass and volume as the LEU cube) in a stopped track radiograph and muon induced fission radiograph. Scintillator bars were located adjacent to the uranium volumes in order to detect the gamma and neutron signals originating from the targets. These signals are then fed into the MMT in a similar way as the previous experiments that utilized the “suitcase” He-3 detector. Additionally, the “suitcase” was also connected to the MMT, but it was located at a sufficient distance from the objects and was not included in this analysis. After post-processing the LEU shows a slightly stronger signal than the DU, but this difference is small. The signal to noise ratio is approximately the same between the raw stopped tracks and the coincidence tracks.

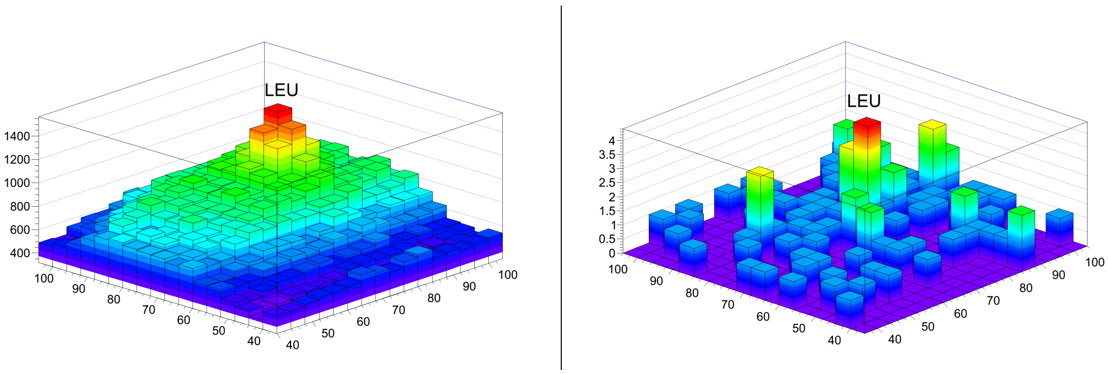

Figure 14 - ROOT and post-processed data showing the LEU cube before (left) and after (right) coincident filtering. This was using the "suitcase" for coincidence detection. The signal to noise ratio is only slightly improved from a peak of 1400:600 to 4:1.

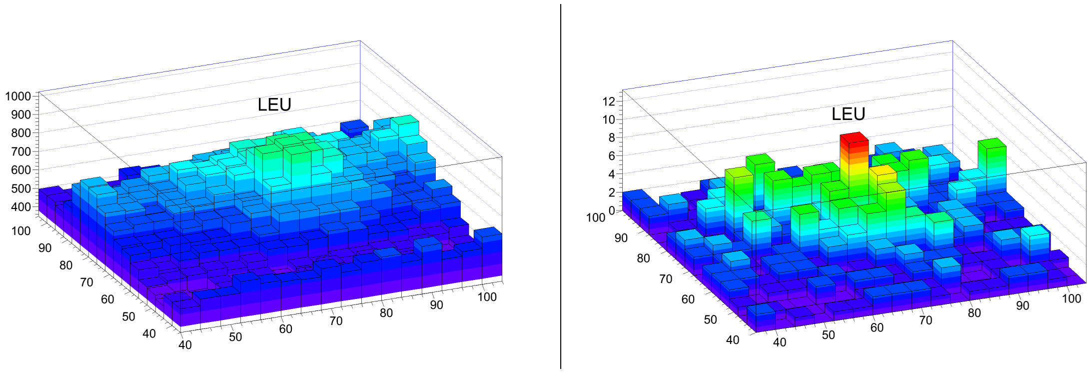

Figure 15 - ROOT and post-processed data showing the LEU cube before (left) and after (right) coincident filtering. This was using the "suitcase" for coincidence detection. The cube was on a stand placing it toward the mid-plane of the detector. The signal to noise ratio for this scenario is slightly improved from 1000:600 to 12:4.

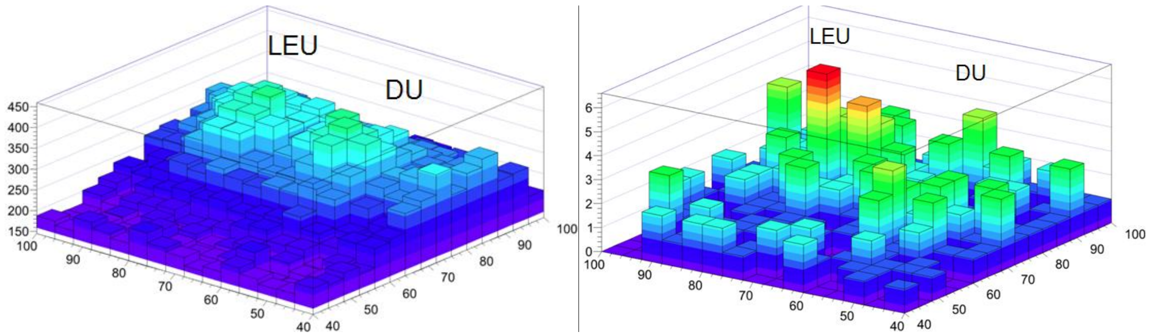

Figure 16 - ROOT and post-processed data showing the LEU and DU peaks before (left) and after (right) coincident filtering. This was using the "suitcase" for coincidence detection.

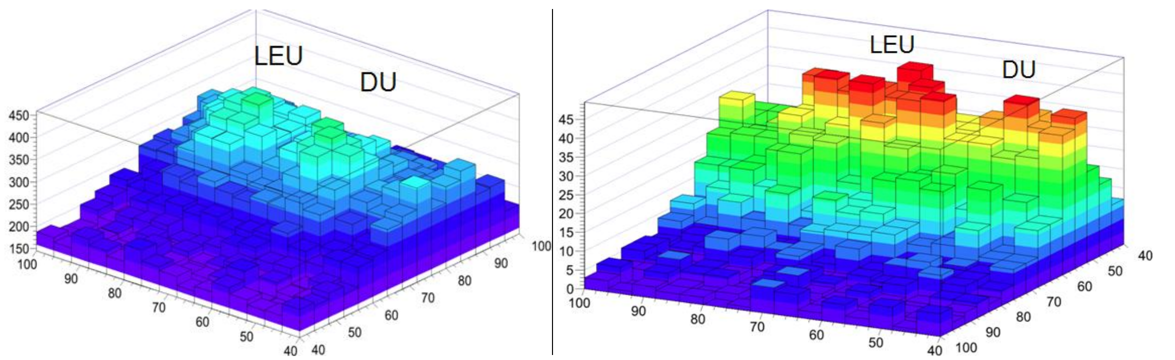

Figure 17 - ROOT and post-processed data showing the LEU and DU peaks before (left) and after (right) coincident filtering. This was using the scintillator bars for coincidence detection.

Measuring Muon Induced Fission in Uranium: LEU and DU, with EJ-301 detectors

We used the MMT for experimental measurements of muon induced fission in 1 liter uranium cubes. Two cubes were studied including a depleted uranium cube (DU) and a 19.5% U-235 enriched uranium cube (LEU). The LEU cube consists of 4 uranium plates bound in a thin steel structure for criticality safety purposes. Two EJ-301 liquid scintillator detectors were located approximately 10 centimeters from the face of the uranium cube. A Mesytec MPD-4 pulse shape discriminator separated neutrons from the gamma background, and the discriminated neutron TTL signal was injected into the MMT data stream. The cubes were measured individually: 23.5 hours for the DU cube and 48 hours for the LEU cube. Multiple scattering reconstructions show the experimental setup in Figure 18.

The stopped track radiography is created before the tagged coincidence image. This is done by measuring events that do not create hits in the bottom supermodule of the MMT. Both of the stopped images are shown in Figure 19. The stopping image has poorer edge resolution when compared to the resolution of multiple scattering. This is due to the wide angle scattering that occurs in softer, high dE/dx muons. There is also a large penumbra due to having many events that miss the bottom supermodule at the edge of the field of view. The stopped track radiography is filtered with a coincidence window containing secondary signals which enables the tagging of muon induced fission.

Two EJ-301 liquid scintillator detectors were used for the measurement of fast neutrons resulting from muon induced fission. This liquid scintillator, made by Eljen Technology, has excellent pulse shape discrimination properties, and it is identical to the well recognized liquid scintillator, NE-213. The scintillator is packaged in a right cylinder with an outer diameter of 12.7 cm and a 2.54 cm thickness. Each scintillator was connected to a Hamamatsu photomultiplier tube (PMT) with a voltage between -1300 V and -1400 V. Both detectors were gain matched with a Cs-137 source photopeak of ~50 mV. The pulse shape discrimination was tested with several gamma sources (including the Cs-137 source) and a Cf-252 neutron source. Following detector calibration, the output of the detectors' neutron discrimination was injected into the MMT data stream. The secondary signals measured by the EJ-301 were clocked with a 200MHz frequency (a temporal resolution of 5 ns).

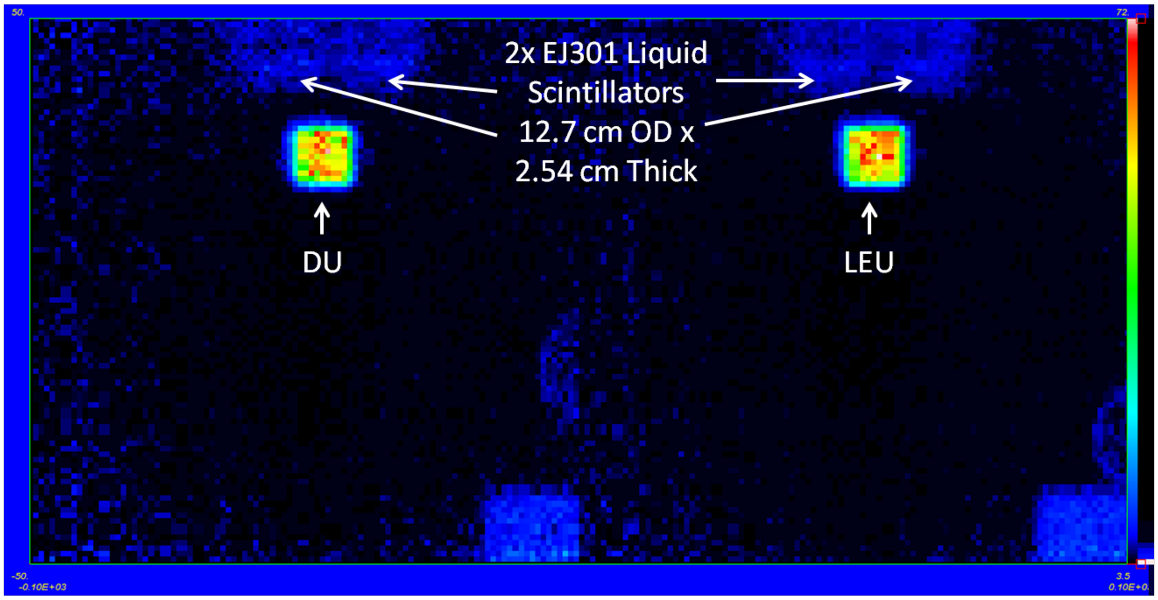

Figure 18 – Multiple scattering measurement of DU (23.5 hours, left) and LEU (48 hours, right). The cubes were placed in a nearly identical location for purposes of comparing stopped tracks and tagged stopped tracks. Several objects in the bottom right corner are extraneous to the scene.

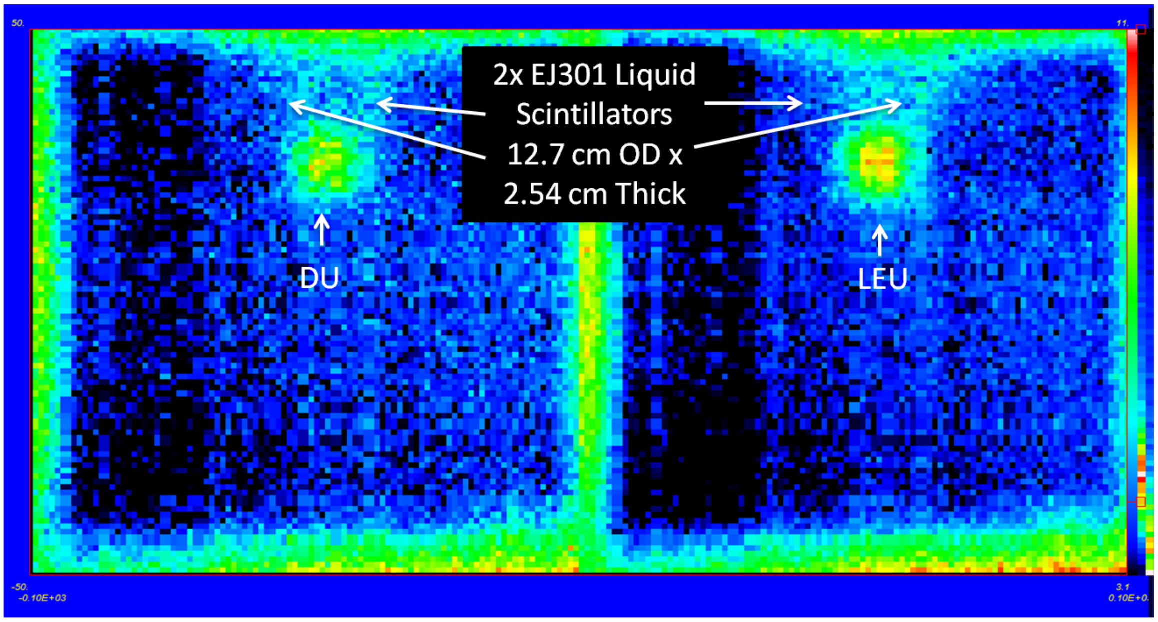

Figure 19 – Stopped track radiography of DU (23.5 hours) and LEU (48 hours) cubes. Both images are normalized to the duration of measurement. The stopped track radiography is the first step in performing coincidence tagged radiography.

The coincidence signal gate width was set between 350 ns and 650 ns for both the LEU and DU runs. This was determined by recording the difference in time stamps between each EJ-301 detector hit and the stopped muon track within a microsecond. Only the first and nearest event was included. Given that the measured rate of coincidence is low, $\sim 10^{-3}\,\frac{\mathrm{n}}{stopped\ \mu}$, the probability of consecutive non-related coincidences occurring in the window is negligible, $10^{-3} * 10^{-3} \rightarrow 10^{-6}$. This ensures that looking for the first, nearest event is adequate for short time windows with infrequent events. The results of the timing spectrum are shown in Figure 20 and Figure 21. For both cube measurements, the detectors returned a peak of hits between 350 ns and 650 ns. It was assumed that the timing distribution was composed of prompt and delayed components of muon induced fission. With this model, the prompt component was fitted with a Gaussian with a width corresponding to system time resolution. The delayed component, which indicates the lifetime of the muonic atom, was fitted using the exponential. The total temporal distribution of events was fitted using a sum of three components: exponential decay, Gaussian, and constant background.

$$y = B + Pe^{-\left(\frac{t-t_0}{\tau}\right)} + Ae^{-\frac{(t-t_0)^2}{2\sigma}} \qquad \text{eq. 2}$$

Where B is a constant background, P is an amplitude at some peak time of the exponential decay, t_0 is the peak location for both the Gaussian and exponential curve, τ is the exponential lifetime associated with the muon capture lifetime, and σ is the Gaussian width.

The lifetime of the muon capture in uranium was measured for each cube. In the literature, the lifetime of muonic U-235 is ~72 ns and in U-238 is ~77 ns [32]. A Poisson distribution was assumed for the data, and the temporal distribution was fitted. The fitting parameters were varied in order to minimize a summed log likelihood ratio, which accounts for statistical weightings near zero counts. This was done using Excel’s solver function while the peak time location, t_0, was fixed. Eighty-seven degrees of freedom were used in the summation that was minimized by the solver.

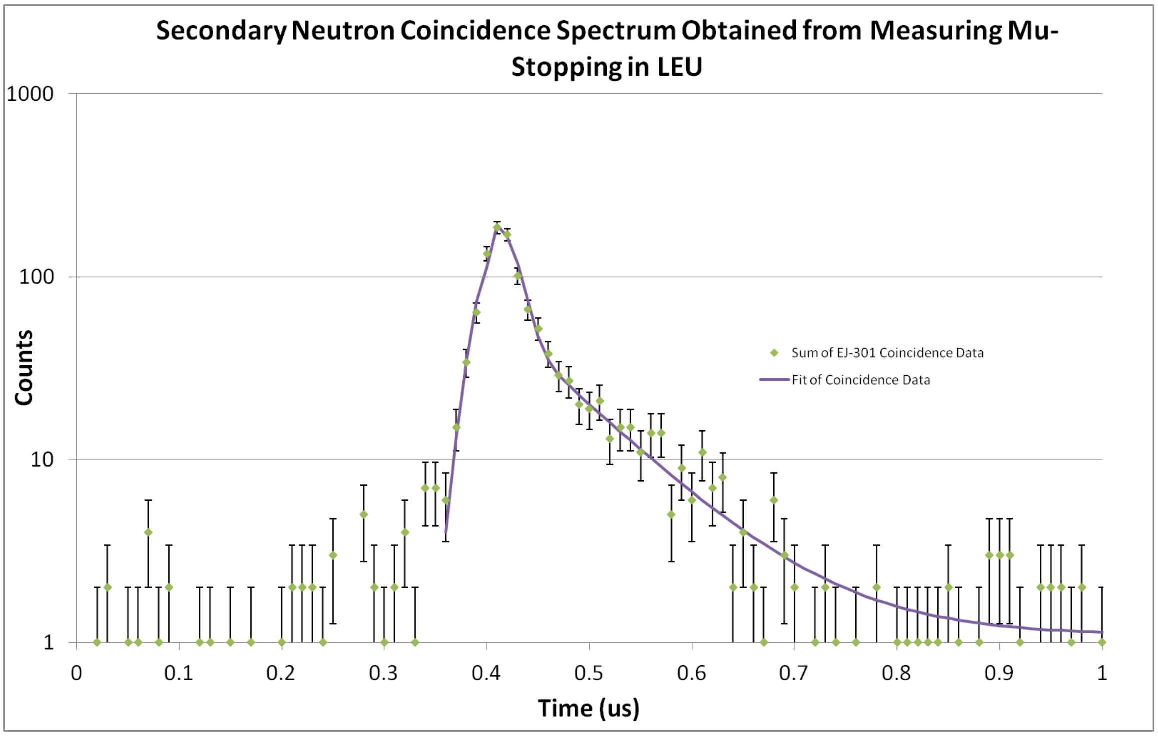

Figure 20 – Secondary neutron coincidence spectrum obtained from a coincidence window of EJ-301 neutron detection and stopped muon tracks in LEU. The data from both detectors is summed (green diamonds) and a log likelihood fit (purple line) is performed on the tail of the coincidence spectrum. The lifetime of the muonic LEU, which is measured by this fit, is $82 \pm 34\ ns$.

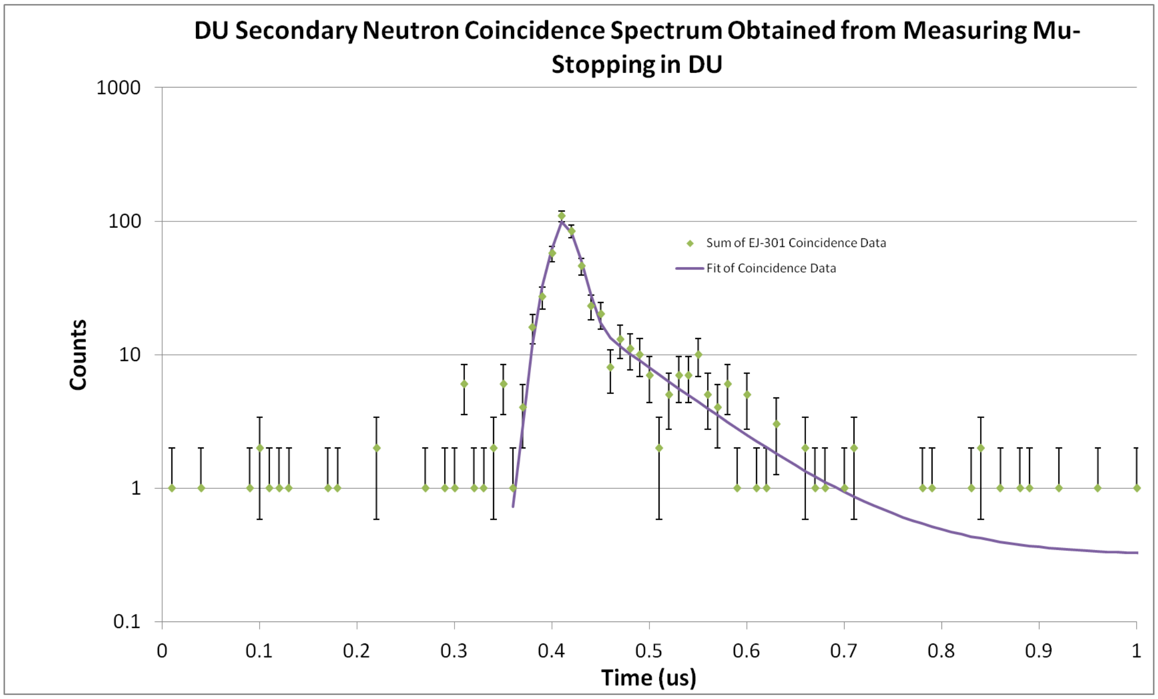

Figure 21 - Secondary neutron coincidence spectrum obtained from a coincidence window of EJ-301 neutron detection and stopped muon tracks in DU. The data from both detectors is summed (green diamonds) and a log likelihood fit (purple line) is performed on the tail of the coincidence spectrum. The lifetime of the muonic DU which is measured by this fit, is $80 \pm 57\ ns$.

The fitted lifetime for the LEU cube was $82 \pm 34\ ns$, and the fitted lifetime for the DU cube was $80 \pm 57\ ns$. The error was determined by computing the 1σ equivalent of a log-likelihood ratio and subtracting the difference between this new lifetime value and the minimized log-likelihood value. Both fits agreed well within the data, with a summed log likelihood (Appendix D) that was approximately equal to the 87 degrees of freedom. Table 2 shows the fitting parameters for both cubes.

The tagged radiography of the LEU and DU cubes are shown in Figure 22. The tagged images were normalized to the total number of stopped tracks, 1.041E+5 stopped tracks in the LEU cube over 48 hours and 4.991E+4 tracks in the DU over 23.5 hours. The total tagged stopped tracks, determined from the neutron detection in coincidence with stopped muons, were 846 ± 29 tracks in the LEU and 376 ± 20 tracks in the DU. This signal contributed statistical error of approximately 4% in LEU and 6% in DU. Following normalization, this amounted to $(7.53 \pm 0.45) \cdot 10^{-3} \frac{\mathrm{n}}{stopped\ \mu}$ in DU and $(8.13 \pm 0.33) \cdot 10^{-3} \frac{\mathrm{n}}{stopped\ \mu}$ in LEU. The relative difference between these two quantities is ~8 percent (see Table 3). This is consistent with our expectation that there should be more neutronics signal from the LEU cube following a stopped muon induced fission. The results of our simulations indicate that if HEU was compared to DU or LEU the signal would be dramatically increased. The tagged muon-induced radiography greatly improves the signal-to-noise ratio of the uranium in the image while being more sensitive to materials with neutronics gain. This feature enables SNM to be identified from inert high-Z materials which is indistinguishable with multiple scattering and transmission radiography.

A simulation was performed using Geant4 of the LEU and DU cube to check agreement between the simulation and data of muon induced fission. The geometry of the simulation is shown in Figure 23. One million isotropic 1 MeV μ^{-} were generated uniformly in each cube, and the neutrons were recorded passing through each cylindrical detector plane. The results of this simulation were used to estimate the efficiency of the EJ-301 detectors by comparison with the measured, tagged data (see

Table 4). The number of neutrons observed per μ^- in the simulation was $0.106\ \frac{\mathrm{n}}{\mu^-}$ in DU and $0.120\ \frac{\mathrm{n}}{\mu^-}$ in LEU.

	DU - Minimized Fit	DU - 1 Sigma	LEU - Minimized Fit	LEU - 1 Sigma
Background (counts)	0.3	0.3	1.1	1.1
Gaussian Amplitude (counts)	75	75	133	133
Gaussian Width (ns)	16	16	18	18
Exponential Amplitude (counts)	24	24	57	57
Exponential Lifetime (ns)	80	137	82	116
Peak Center (ns)	410	410	410	410
Degrees of Freedom	87	87	87	87
Summed Log-Likelihood	81	168	87	164
Lifetime Uncertainty (ns)	57	57	34	34

Table 2 – Fit parameters of temporal distributions for a liquid-scintillator measuring neutrons in coincidence with stopped muons. The measured lifetime of the muon capture in uranium was $82 \pm 34\ ns$ in LEU and $87 \pm 57\ ns$ in DU. The DU measurement had nearly half the total counts of the LEU measurement.

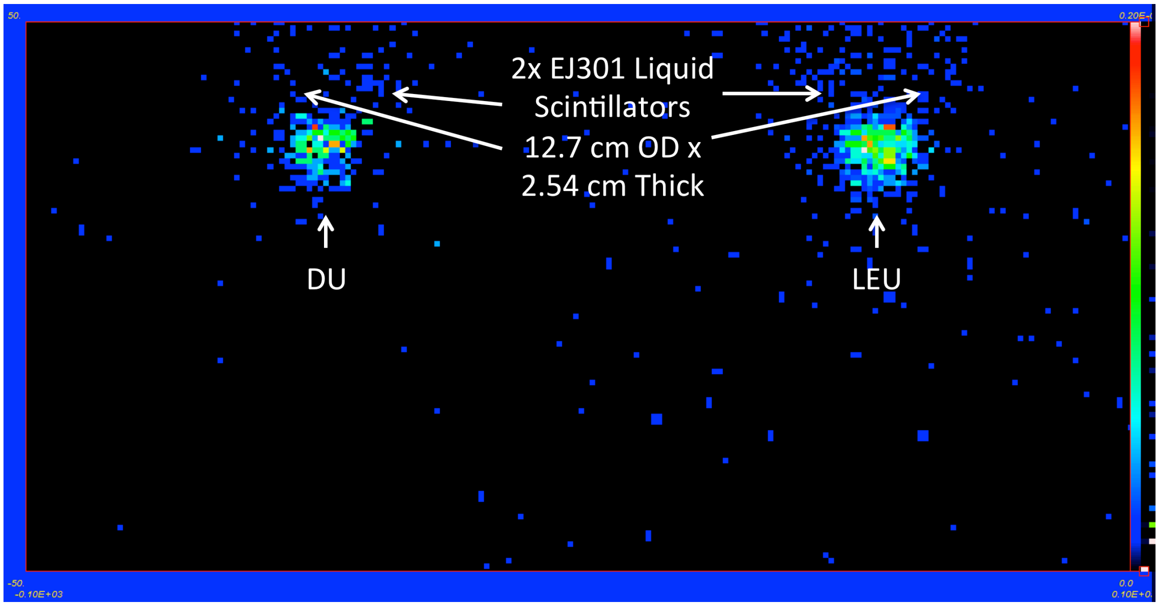

Figure 22 – Tagged radiography in coincidence with muon induced fission neutrons. The signal in the LEU cube is approximately 8 percent stronger which indicates the presence of neutronics gain from the U-235 enrichment. The detectors are barely present in the field of view after performing the tagged radiography.

Cubes	DU	LEU
Measurement Duration (min)	1410	2880
Stopped Tracks (counts)	4.99E+04	1.04E+05
Stopped Tracks (counts/min)	3.54E+01	3.61E+01
Tagged Stopped Tracks (counts)	376	846
Tagged Stopped Tracks (counts/stopped)	7.53E-03	8.13E-03

Table 3 – Two measurements of uranium cubes were made with the MMT. For each cube, the number of stopping tracks in the cube's location is shown. The tagged stopped tracks are shown as well and are normalized by the total amount of stopped tracks in the cube. Thus, we measure a fission neutron signal of smaller than 1 percent of the stopped muons in the uranium cubes.

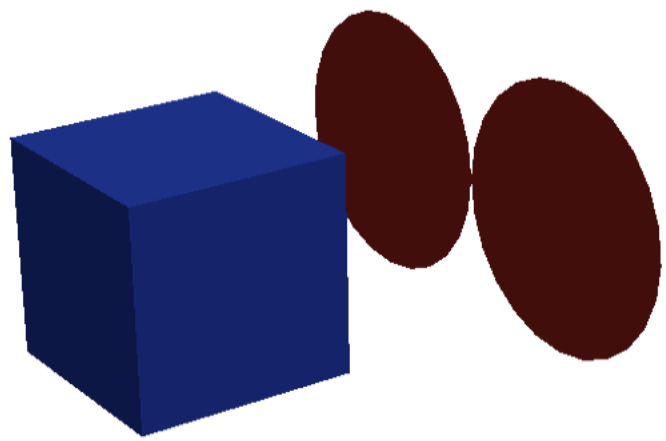

Figure 23 – Simulation geometry used in Geant4 to model muon induced fission measured by two cylindrical detector planes representing EJ-301 liquid scintillators.

Cubes	DU	LEU
Sim: Neutrons Detected (counts)	1.06E+05	1.20E+05
Sim: Neutrons Detected (counts/mu-)	1.06E-01	1.20E-01
Mu Minus Ratio (mu-/mu)	0.45	0.45
Sim: Neutrons Detected (counts/mu)	4.78E-02	5.38E-02
Tagged Stopped Tracks (counts/mu)	7.53E-03	8.13E-03
Predicted Detector Efficiency	1.58E-01	1.51E-01

Table 4 – This table contains the results of a Geant4 simulation used to check the approximate amount of neutrons expected. The geometry of the simulation is shown in Figure 23. The table shows the normalized amount of neutrons detected as a function of the stopped μ^- flux. This value is then renormalized to compare to the total stopped flux measured in data to approximate a detector efficiency of ~15-16 percent.

These values were then normalized assuming that the μ^- constituted 45 percent of the total cosmic-ray muon flux. The detector efficiency for the EJ-301 detectors was then computed to be ~15-16 percent. This compares well with published literature values (i.e. NE-213 efficiencies) [33-36].

For practical implementation of one sided imaging, we cannot rely on the knowledge of whether the cosmic-ray muon was stopped in the object. Therefore, the total signal of single sided imaging is composed of both stopped and transmitted muons. The results of the cosmic-ray muons stopping in cubes of LEU and DU have been shown along with the tagged component associated with stopped muon induced fission. The transmission of cosmic-ray muons has also been analyzed, shown in Figure 24; there are $2.29 \cdot 10^5$ muons transmitted through the LEU cube and $1.13 \cdot 10^5$ muons through the DU cube (see Table 5). A coincidence window was established with the transmitted tracks between 350 ns and 460 ns. The temporal distribution of the coincidence data between the transmitted muons and secondary signal is prompt (see Figure 25 and Figure 26). This is expected due to the prompt nature of muon Bremsstrahlung induced secondary neutrons. The measurement of the prompt width is similar to that of the prompt component seen in the stopped μ^- temporal distribution which was fit with a Gaussian model. The lack of a tail in the transmitted muon coincidence spectrum reinforces our explanation of the lifetime observed from measuring the stopped muon coincidence spectrum.

There were 141 ± 12 neutrons measured in coincidence with the LEU cube and 60 ± 8 neutrons measured in coincidence with the DU cube. This amounts to a coincidence rate of $(5.3 \pm 0.7) \cdot 10^{-4} \frac{\mathrm{n}}{trans.\ \mu}$ in DU and $(6.1 \pm 0.5) \cdot 10^{-4} \frac{\mathrm{n}}{trans.\ \mu}$ in LEU. The simulations predict that the transmitted signal should be closer to 1 percent of the stopped tracks instead of the 10 percent measured in the data. This difference is not understood at this point and will be explored in the future, requiring more accurate simulation of the physics and geometry. The combined tagged radiography, containing both the stopped and transmitted components, is shown in Figure 27. Figure 27 is similar to

Figure 22 because the majority of the muon induced fission signal arises from stopped μ^-. The tagging of stopped and transmitted tracks proves that muon induced fission imaging is possible.

We developed a methodology for single sided imaging using cosmic-ray muons in coincidence with secondary signals. Simulations were studied of the neutronics in uranium, muon induced fission output, and experimental geometry. The experimental data was consistent with our expectations derived from the simulations. Our study confirms the feasibility of single sided imaging in coincidence with muon induced fission for identifying and imaging SNM.

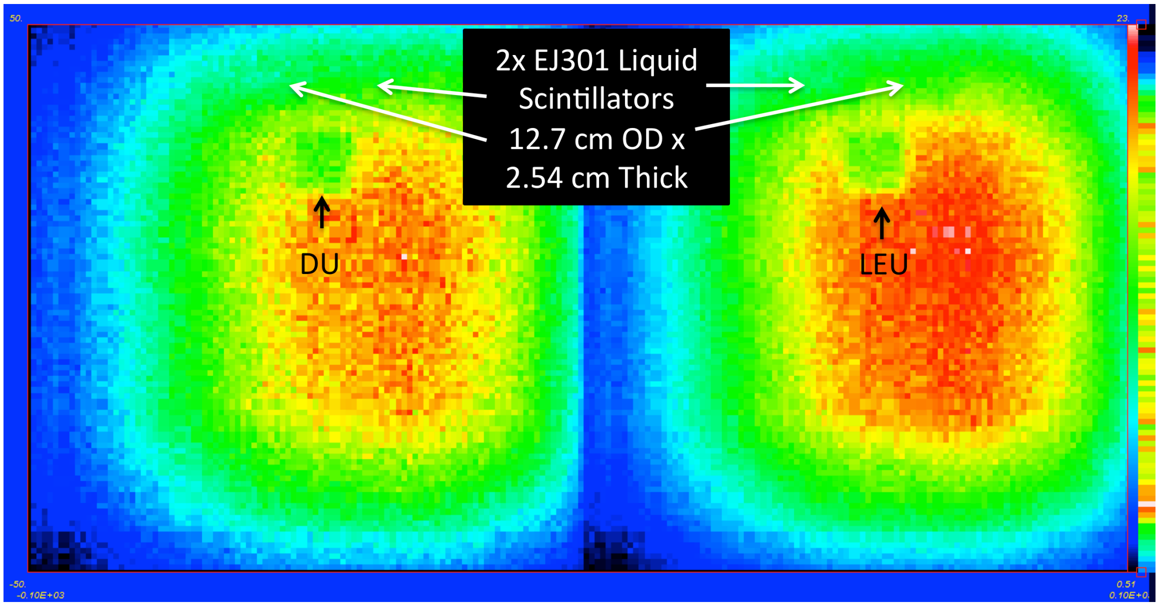

Figure 24 – Cosmic-ray muon transmission reconstruction of the DU and LEU cubes. This image shows the shadow of each cube where the missing flux is due to muons stopping in the uranium. The DU was measured for 23.5 hours and the LEU was measured for 48 hours. Both images have been normalized to the time measured, and the difference in statistics between the two measurements is noticeable when comparing the smoothness of the LEU data to the DU data.

Cubes	DU	LEU
Measurement Duration (min)	1410	2880
Transmitted Tracks (counts)	1.13E+05	2.29E+05
Transmitted Tracks (counts/min)	8.02E+01	7.97E+01
Tagged Transmitted Tracks (counts)	6.00E+01	1.41E+02
Tagged Transmitted Tracks (counts/Transmitted Mu)	5.31E-04	6.15E-04
Tagged Stopped Tracks (counts/Stopped Mu)	7.53E-03	8.13E-03
Total Tagged Tracks (counts/Mu)	8.06E-03	8.74E-03

Table 5 – This table summarizes the amount of tagged tracks seen in the data for the uranium cube measurements. The total tagged tracks are a summation of the tagged tracks observed from both muon stopping and transmission. There is ~8 percent increase in signal found in the normalized total tagged tracks from the LEU.

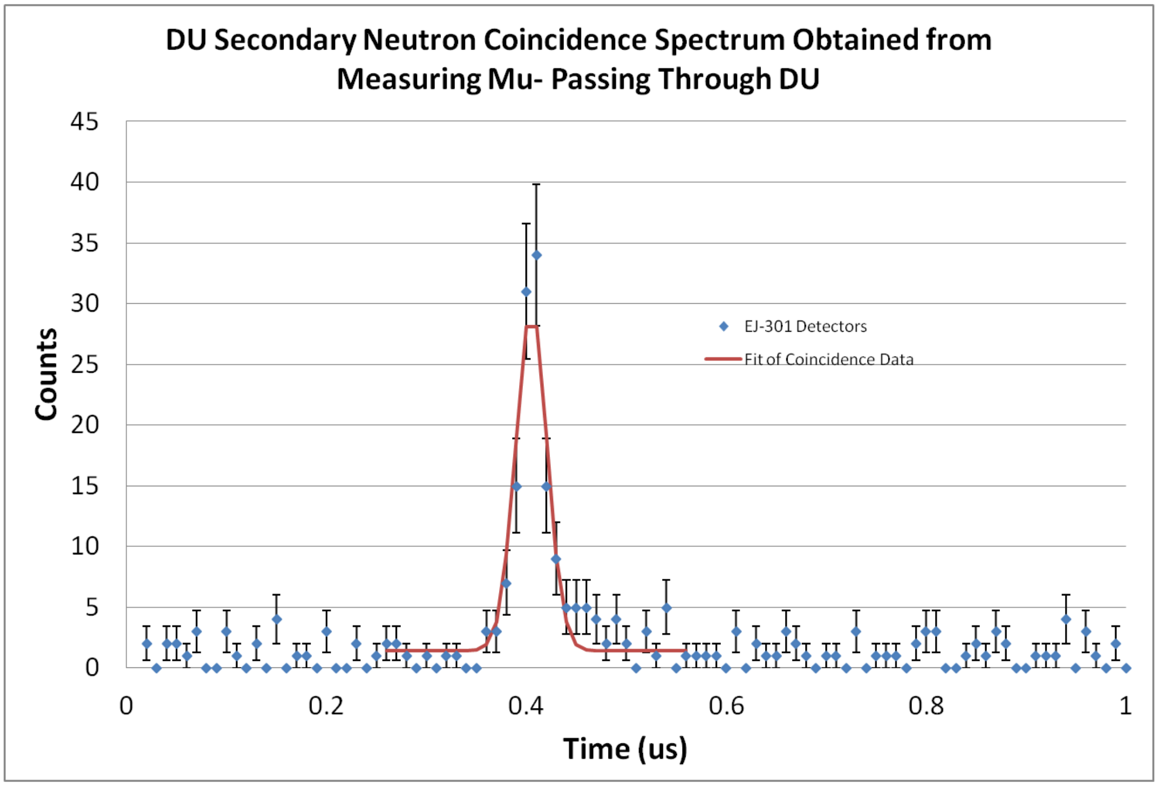

Figure 25 – Secondary neutron coincidence spectrum obtained from a coincidence window of EJ-301 neutron detection and transmitted muon tracks in DU. The data from both detectors is summed (blue diamonds) and a log likelihood fit (red line) using a Gaussian model is applied to the data. The width of the Gaussian is 16 ns.

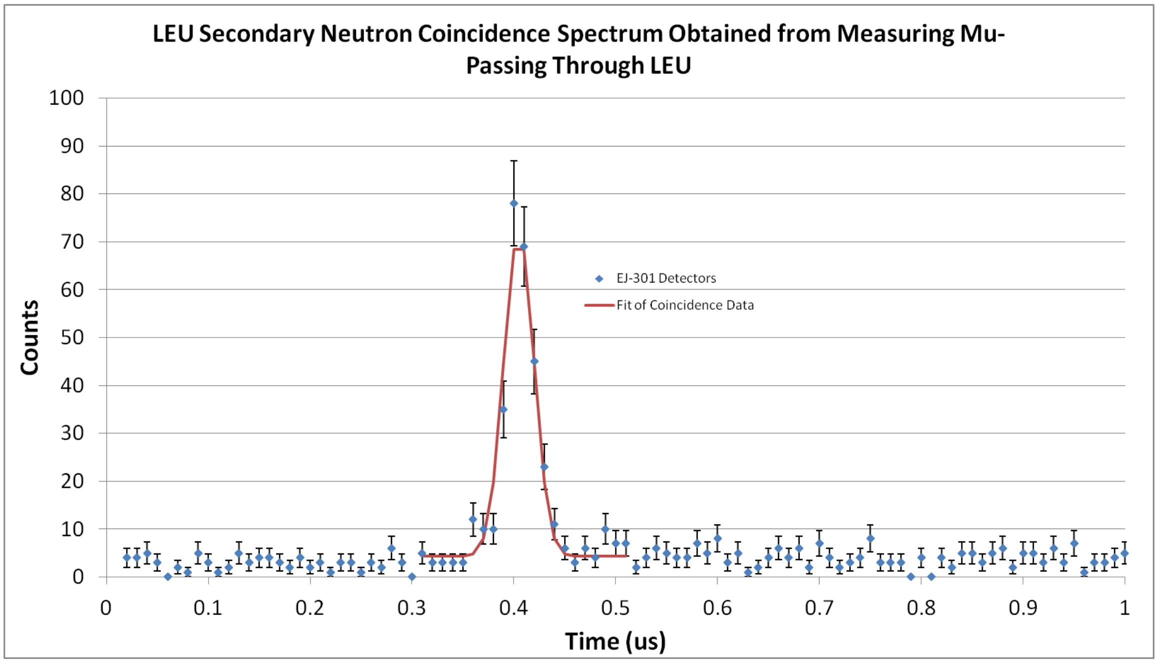

Figure 26 - Secondary neutron coincidence spectrum obtained from a coincidence window of EJ-301 neutron detection and transmitted muon tracks in DU. The data from both detectors is summed (blue diamonds) and a log likelihood fit (red line) using a Gaussian model is applied to the data. The width of the Gaussian is 15 ns.

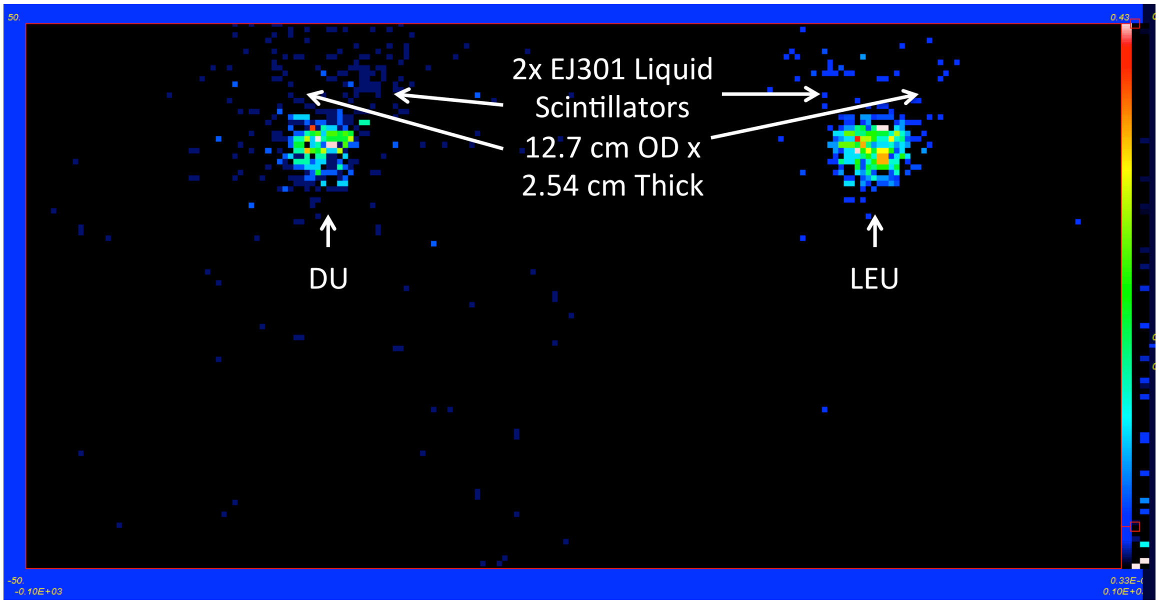

Figure 27 - Tagged radiography in coincidence with cosmic-ray muons that stop and transit through the uranium cubes. The total signal in the LEU cube is approximately 8 percent stronger which indicates the presence of neutronics gain from the U-235 enrichment. The detectors are barely present in the field of view after performing the tagged radiography.

Horizontal vs. Vertical Imaging with Cosmic Ray Muons

Sixty nine hours of data have been taken in a horizontal viewing mode configuration to compare with a vertical data set taken with the same object (pending publication in NIM). Photographs of the scanner in both its vertical and horizontal viewing modes are shown in Figure 28 .

The counting rate taken in both the horizontal and vertical viewing modes are plotted in Figure 29 as a function of azimuthal angle. The curve plotted as a solid line has been fitted to the data and is given by:

$$\frac{dN}{d\Omega dt} = 0.66\cos^2(\theta)\,(\mathrm{sr}^{-1}\mathrm{cm}^{-2}\mathrm{min}^{-1}),$$

where *N* is the number of tracks detected, *Ω* is the solid angle, *t* is time. Integrating over the upper hemisphere gives a total flux of 1.4 muon $cm^{-1}min^{-1}$ consistent with a higher flux than is measured at sea level of 1.0 muon $cm^{-1}min^{-1}$ because of the elevation of Los Alamos of 2200 m above sea level. The data can be seen to fall lower than the curve as one moves away from the center of the acceptance (0 for vertical mode and $\pi/2$ for horizontal viewing mode) because of the finite thickness of the tracking detectors which results in a loss of tracking efficiency near the edges for non-normal incident trajectories. The angular distribution, which goes to zero at the horizon, illustrates the reason for the concerns about the times needed for horizontal viewing mode imaging, because the horizontal track rate is approximately a factor of 10 lower than the track rate in vertical viewing mode-in agreement with expectations.

The time development of the reconstructions is shown in Figure 30) for the two imaging modes. In these plots the z direction is along the bisector of the detectors and the x-y plane is parallel to the detector faces. It takes about 1 hour of exposure to distinguish the inner cavity of the lead ball in vertical mode and about 8 hours in horizontal viewing mode. This is most apparent in the upper row of each set of data, where the Abel inversion of the center x-y slice is shown.

Results from the one-dimensional reconstruction are shown in Figure 31 and Figure 32, where the radiation length areal and volume densities are plotted respectively as a function of radius. It is possible to identify and measure the inner radius with exposures of about 15 minutes and 4 hours in vertical and horizontal viewing modes respectively.

In actual use the detectors need not be constrained to the geometries used here. In horizontal viewing mode, introducing a vertical offset between the detectors can increase the counting rate because it reduces the average azimuthal angle. This is countered by a reduction in the average solid angle because the detectors are on average further from the object. In order to study these effects we have numerically integrated $\frac{dN}{d\theta}d\Omega$ over a detector plane for both horizontal and vertical viewing modes.

Figure 28)Left: photograph of the muon scanner in vertical viewing mode. Right: photograph of the scanner in horizontal viewing mode with the lead sphere in place.

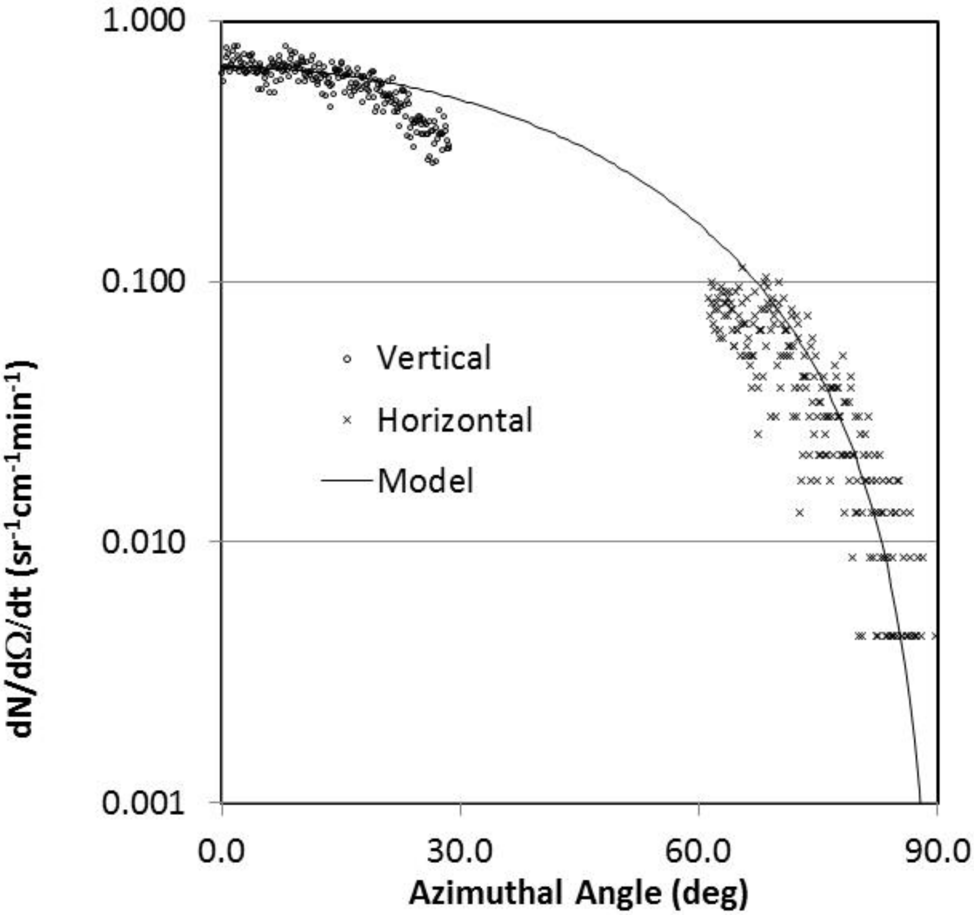

Figure 29) Normalized counting rate as a function of azimuthal angle taken in the two modes of operation compared to the model given in the text.

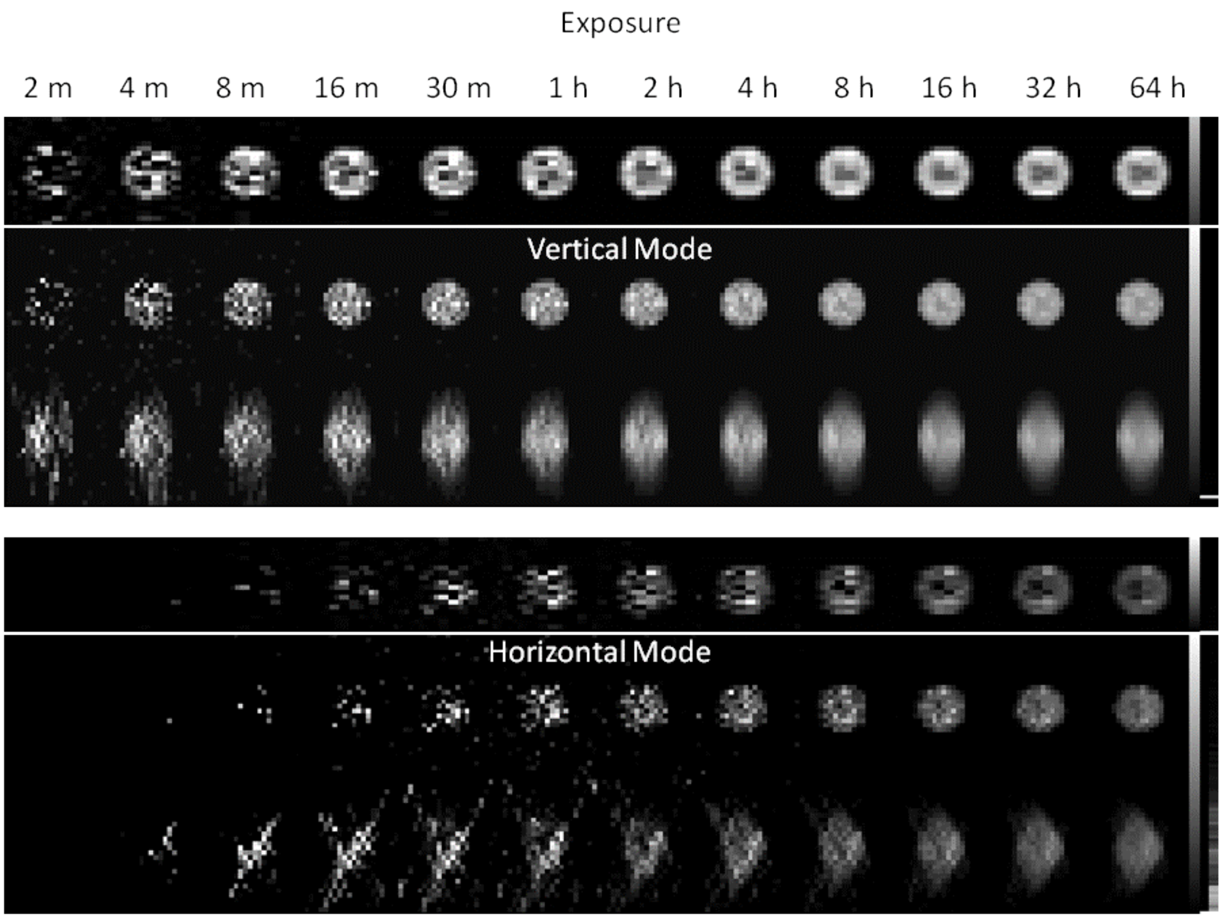

Figure 30) Images of the reconstructed images in vertical viewing mode (top) and horizontal viewing mode (bottom) For each mode there are three rows of images as a function of exposure time on an approximate geometric time scale. Bottom row is an x-z slice and the middle row is an x-y slice from the tomographic reconstruction, and the top row is an Abel inversion of the x-y slice.

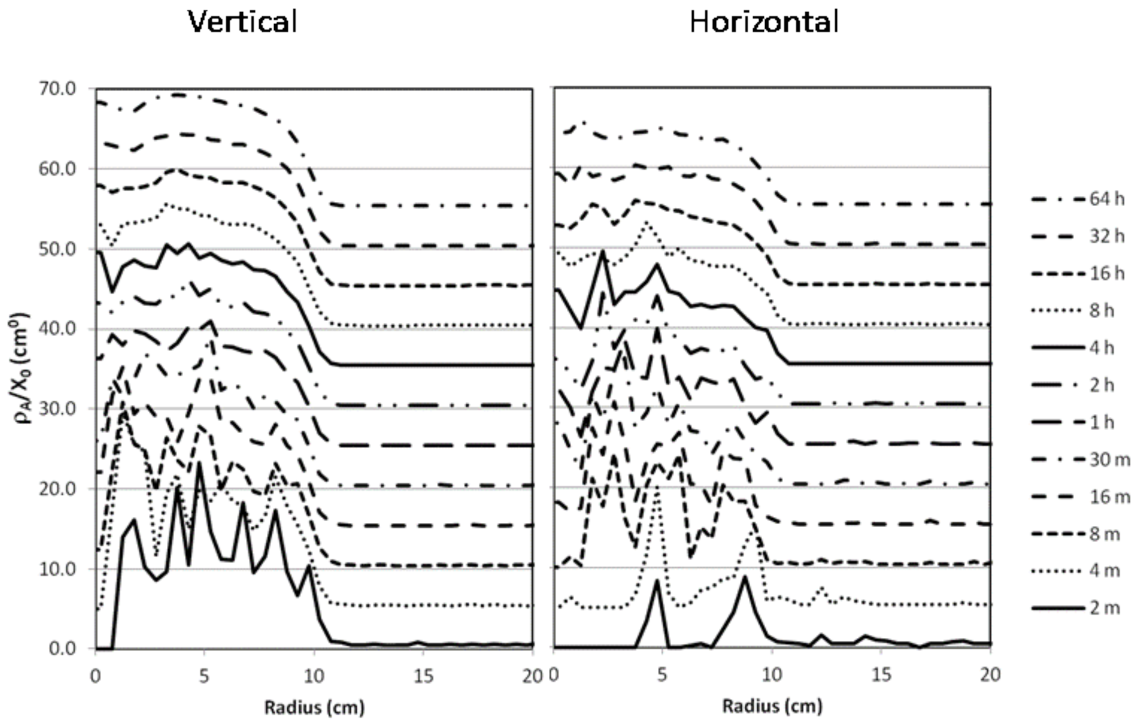

Figure 31) Radiation length weighted areal density obtained in vertical (right) and horizontal (right) viewing modes. The curves at different times are offset from one another for clarity.

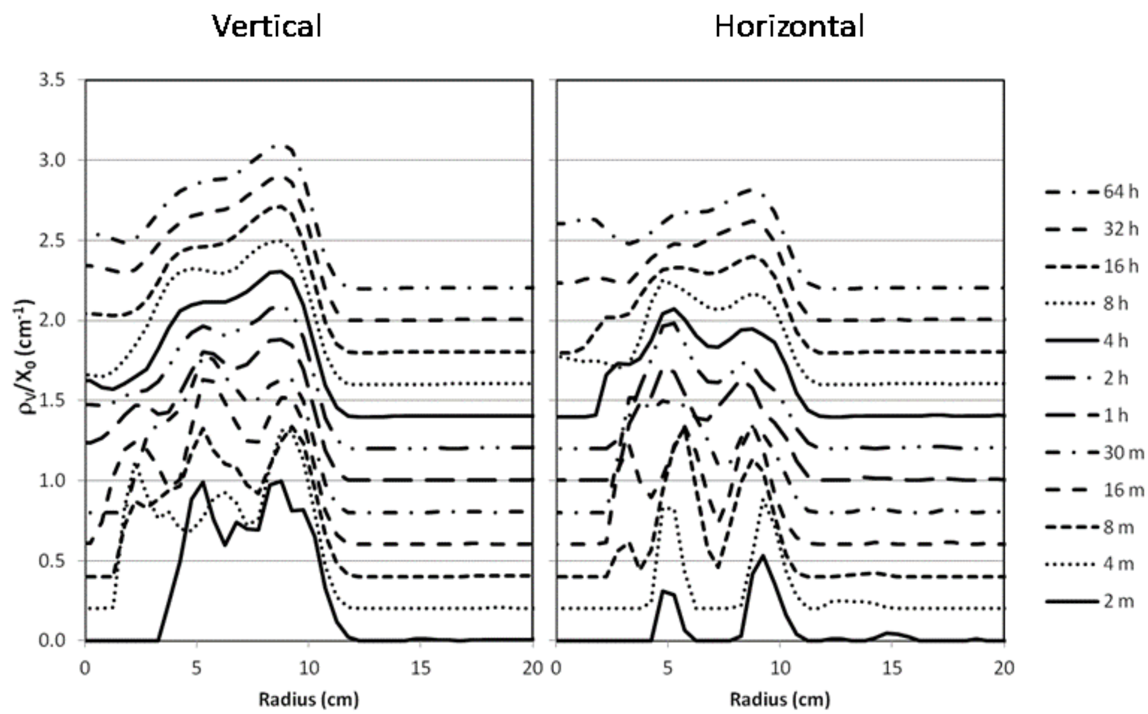

Figure 32) Abel Inversions of the data presented in Figure 31. The results are radiation length weighted volume density. Succeeding plots are offset by 0.2 cm^{-1}.

In Figure 33, the balance between vertical offset and solid angle for the horizontal viewing mode is apparent in this plot. For the simple geometry, studied here, a vertical offset equal to the detector size gives a factor of three increase in counting rate over the geometry with no offset. A further gain can be obtained by moving the detectors closer to the object. Here we argue that by using smaller diameter drift tubes (25 cm vs. 50 cm), which makes the tracker thinner, the tracker can be placed at an average closer distance with increased solid angle. With better geometries the counting rate can be increased by ~5 for vertical geometries over the case used here.

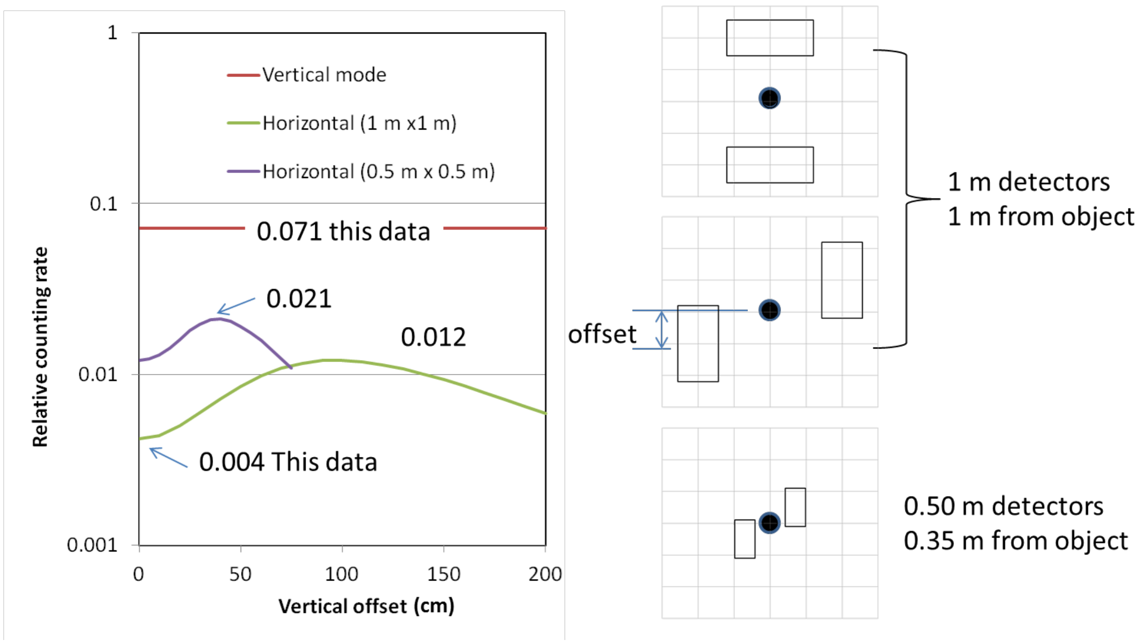

Figure 33) On the left the integrated flux through an object centered in the field of view for the geometries schematically illustrated on the right. In the illustrations the boxes show the outer dimensions of the tracking modules and the grid has a pitch of 0.5 m.

Conclusions

We developed a methodology for single sided imaging using cosmic-ray muons in coincidence with secondary signals. Simulations were studied of the neutronics in uranium, muon induced fission output, and experimental geometry. Both the prompt and delayed temporal neutron coincidence distributions were measured from muons interacting in uranium. The delayed component of the stopped μ^- induced fission was measured at ~80 ns in uranium. The prompt component of this coincidence timing spectrum was measured for muons that stopped and transmitted in the cubes of DU and LEU. The experimental data was consistent with our expectations derived from the simulations. Our study confirms the feasibility of single sided imaging in coincidence with muon induced fission for identifying and imaging SNM. It was shown that for single sided imaging, with our EJ-301 secondary detector configuration, we measured an SNM tagging rate of $8.06 \cdot 10^{-3} \frac{\mathrm{n}}{\mu}$ in DU and $8.74 \ \cdot 10^{-3} \frac{\mathrm{n}}{\mu}$ in LEU. Simulations suggest that HEU would show an increase in secondary neutrons by a factor of 2 as compared to the LEU or DU. Advancements in detector design, through the use of carbon fiber drift tubes and solid plastic pulse-shape discrimination neutron detectors, allow for a lightweight, field deployable muon induced fission detector with a safe alternative to low-flashpoint volatile organics. Finally, the horizontal component of muon flux is shown to generate images with the same quality as compared to the vertical flux with an increase in time within an order of magnitude.

References

1. Morris, C.L., et al., *Tomographic imaging with cosmic ray muons.* Science and Global Security, 2008. **16**(1-2): p. 37-53.
2. Klimenko, A.V., et al., *Exploring signatures of different physical processes for fusion with scattering muon tomography.* IEEE Transactions on Nuclear Science, 2007. **54**(1): p. 228-235.
3. Schultz, L.J., et al., *Statistical reconstruction for cosmic ray muon tomography.* IEEE Transactions on Image Processing, 2007. **16**(8): p. 1985-93.
4. Schultz, L.J., et al., *Image reconstruction and material Z discrimination via cosmic ray muon radiography.* Nuclear Instruments & Methods in Physics Research, Section A (Accelerators, Spectrometers, Detectors and Associated Equipment), 2004. **519**(3): p. 687.
5. Borozdin, K.N., et al., *Scattering Muon radiography and its application to the detection of high-Z materials.* IEEE Nuclear Science Symposium ConferenceCRecord, 2004: p. 3444.
6. Borozdin, K.N., et al., *Surveillance: Radiographic imaging with cosmic-ray muons.* Nature, 2003. **422**(6929): p. 277.
7. Hogan, G.E., et al. *Proton radiography.* 1999. Piscataway, NJ, USA : IEEE, 1999.
8. King, N.S.P., et al., *An 800-MeV proton radiography facility for dynamic experiments.* Nuclear Instruments & Methods in Physics Research Section A-Accelerators Spectrometers Detectors and Associated Equipment, 1999. **424**(1): p. 84-91.
9. Cookson, J., *Radiography with protons.* Naturwissenschaften, 1974. **61**(5): p. 184-191.
10. STEWARD, V.W. and A.M. KOEHLER, *Proton radiography as a diagnostic tool.* Physics in Medicine and Biology, 1973. **18**(4): p. 591.
11. Ellard, G.A., et al., *Radiography with 160 MeV protons.* Nature, 1972. **239**(5368): p. 157-9.
12. Cookson, J.A., B.H. Armitage, and A.T. Ferguson, *Proton radiography.* Non-Destructive Testing, 1972. **5**(4): p. 225-8.
13. KOEHLER, A.M., *PROTON RADIOGRAPHY.* Physics in Medicine and Biology, 1970. **15**(1): p. 181-&.
14. KOEHLER, A.M., *Proton radiography.* Science, 1968. **160**(3825): p. 303-4.
15. Kaufman, L. and J. Carlson, *An evaluation of airport x-ray backscatter units based on image characteristics.* Journal of Transportation Security, 2011. **4**(1): p. 73-94.
16. Warren, G.A., et al., *On the Search for Nuclear Resonance Fluorescence Signatures of U-235 and U-238 Above 3 MeV.* Ieee Transactions on Nuclear Science, 2010. **57**(1): p. 317-322.
17. Warren, G.A., et al., *Nuclear resonance fluorescence of U-235 above 3 MeV.* 2007 Ieee Nuclear Science Symposium Conference Record, Vols 1-11, 2007: p. 2047-2049.
18. Warren, G.A., et al., *Nuclear Resonance Fluorescence of (235)U.* 2006 Ieee Nuclear Science Symposium Conference Record, Vol 1-6, 2006: p. 914-917.
19. Johnson, M.S., et al., *Applications of Photonuclear Physics for International Safeguards and Security.* Journal of the Korean Physical Society, 2011. **59**(2): p. 1414-1417.
20. Bertozzi, W., et al., *Accelerators for Homeland Security.* International Journal of Modern Physics A, 2011. **26**(10-11): p. 1713-1735.
21. Bertozzi, W., et al., *Imaging and Radiography with Nuclear Resonance Fluorescence and Effective-Z (EZ-3D (TM)) Determination; SNM Detection Using Prompt Neutrons from Photon Induced Fission.* Application of Accelerators in Research and Industry, 2009. **1099**: p. 559-564.
22. Bertozzi, W., et al., *Nuclear resonance fluorescence and effective Z determination applied to detection and imaging of special nuclear material, explosives, toxic substances and contraband.* Nuclear Instruments & Methods in Physics Research Section B-Beam Interactions with Materials and Atoms, 2007. **261**(1-2): p. 331-336.

23. Bertozzi, W. and R.J. Ledoux, *Nuclear resonance fluorescence imaging in non-intrusive cargo inspection.* Nuclear Instruments & Methods in Physics Research Section B-Beam Interactions with Materials and Atoms, 2005. **241**(1-4): p. 820-825.
24. Duderstadt, J.J. and L.J. Hamilton, *Nuclear reactor analysis*1976. Medium: X; Size: Pages: 563.
25. Watt, B.E., *Energy Spectrum of Neutrons from Thermal Fission U-235.* Physical Review, 1952. **87**(6): p. 1037-1041.
26. Tepel, J.W., *Ensdf - the Evaluated Nuclear-Structure Data File.* Computer Physics Communications, 1984. **33**(1-3): p. 129-146.
27. Malyshkin, Y., et al., *Neutron production and energy deposition in fissile spallation targets studied with Geant4 toolkit.* Nuclear Instruments & Methods in Physics Research Section B-Beam Interactions with Materials and Atoms, 2012. **289**: p. 79-90.
28. Guardiola, C., et al., *Geant4 and MCNPX simulations of thermal neutron detection with planar silicon detectors.* Journal of Instrumentation, 2011. **6**.
29. Othman, M.A.R., et al., *From imaging to dosimetry: GEANT4-based study on the application of Medipix to neutron dosimetry.* Radiation Measurements, 2010. **45**(10): p. 1355-1358.
30. Jamil, M., et al., *Simulation study using GEANT4 Monte Carlo code for a Gd-coated resistive plate chamber as a thermal neutron detector.* Radiation Measurements, 2010. **45**(7): p. 840-843.
31. Howard, A., et al., *Validation of Neutrons in Geant4 Using TARC Data - production, interaction and transportation.* 2008 Ieee Nuclear Science Symposium and Medical Imaging Conference (2008 Nss/Mic), Vols 1-9, 2009: p. 2160-2164.
32. Hanscheid, H., et al., *Muon-Capture Rates in U-233, U-234, U-235, U-236, U-238, and Np-237.* Zeitschrift Fur Physik a-Hadrons and Nuclei, 1990. **335**(1): p. 1-8.
33. Shin, K., et al., *Measurements of Ne-213 Response Functions to Neutrons of Energies up to Several 10s of Mev.* Nuclear Instruments & Methods in Physics Research Section a-Accelerators Spectrometers Detectors and Associated Equipment, 1991. **308**(3): p. 609-615.
34. Urone, P.P., N.S.P. King, and M.W. Mcnaughton, *Absolute Neutron-Detector Efficiency for Ne-213 from 11 to 50 Mev.* Bulletin of the American Physical Society, 1976. **21**(1): p. 109-109.
35. Drosg, M., *Accurate Measurement of Counting Efficiency of a Ne-213 Neutron Detector between 2 and 26 Mev.* Nuclear Instruments & Methods, 1972. **105**(3): p. 573-&.
36. Odell, A.A., C.W. Sandifer, and R.B. Knowlen, *Efficiency and Charged Particle Response of an Ne-213 Fast-Neutron Detector.* Bulletin of the American Physical Society, 1968. **13**(4): p. 559-&.